



A remote sensing-based model of tidal marsh aboveground carbon stocks for the conterminous United States

Kristin B. Byrd^{a,*}, Laurel Ballanti^a, Nathan Thomas^b, Dung Nguyen^a, James R. Holmquist^c, Marc Simard^b, Lisamarie Windham-Myers^d

^aU.S. Geological Survey, Western Geographic Science Center, 345 Middlefield Road, MS-531 Menlo Park, CA, USA

^bJet Propulsion Laboratory, California Institute of Technology, 4800 Oak Grove Dr., 300-319D Pasadena, CA 91109, USA

^cSmithsonian Environmental Research Center, 647 Contees Wharf Rd, Edgewater, MD 21037, USA

^dU.S. Geological Survey, National Research Program, 345 Middlefield Road, MS-480 Menlo Park, CA, USA

ARTICLE INFO

Article history:

Received 17 August 2017

Received in revised form 16 March 2018

Accepted 19 March 2018

Available online 31 March 2018

Keywords:

Tidal marsh biomass

Aboveground carbon stocks

Plant functional type

National greenhouse gas inventory

Multispectral imagery

C-band synthetic aperture radar

ABSTRACT

Remote sensing based maps of tidal marshes, both of their extents and carbon stocks, have the potential to play a key role in conducting greenhouse gas inventories and implementing climate mitigation policies. Our objective was to generate a single remote sensing model of tidal marsh aboveground biomass and carbon that represents nationally diverse tidal marshes within the conterminous United States (CONUS). We developed the first calibration-grade, national-scale dataset of aboveground tidal marsh biomass, species composition, and aboveground plant carbon content (%C) from six CONUS regions: Cape Cod, MA, Chesapeake Bay, MD, Everglades, FL, Mississippi Delta, LA, San Francisco Bay, CA, and Puget Sound, WA. Using the random forest machine learning algorithm, we tested whether imagery from multiple sensors, Sentinel-1 C-band synthetic aperture radar, Landsat, and the National Agriculture Imagery Program (NAIP), can improve model performance. The final model, driven by six Landsat vegetation indices and with the soil adjusted vegetation index as the most important ($n = 409$, $RMSE = 310 \text{ g/m}^2$, 10.3% normalized RMSE), successfully predicted biomass for a range of marsh plant functional types defined by height, leaf angle and growth form. Model results were improved by scaling field-measured biomass calibration data by NAIP-derived 30 m fraction green vegetation. With a mean plant carbon content of 44.1% ($n = 1384$, 95% C.I. = 43.99%–44.37%), we generated regional 30 m aboveground carbon density maps for estuarine and palustrine emergent tidal marshes as indicated by a modified NOAA Coastal Change Analysis Program map. We applied a multivariate delta method to calculate uncertainties in regional carbon densities and stocks that considered standard error in map area, mean biomass and mean %C. Louisiana palustrine emergent marshes had the highest C density ($2.67 \pm 0.004 \text{ Mg/ha}$) of all regions, while San Francisco Bay brackish/saline marshes had the highest C density of all estuarine emergent marshes ($2.03 \pm 0.004 \text{ Mg/ha}$). Estimated C stocks for predefined jurisdictional areas ranged from $1023 \pm 39 \text{ Mg}$ in the Nisqually National Wildlife Refuge in Washington to $507,761 \pm 14,822 \text{ Mg}$ in the Terrebonne and St. Mary Parishes in Louisiana. This modeling and data synthesis effort will allow for aboveground C stocks in tidal marshes to be included in the coastal wetland section of the U.S. National Greenhouse Gas Inventory. With the increased availability of free post-processed satellite data, we provide a tractable means of modeling tidal marsh aboveground biomass and carbon at the global extent as well.

Published by Elsevier B.V. on behalf of International Society for Photogrammetry and Remote Sensing, Inc. (ISPRS). This is an open access article under the CC BY-NC-ND license (<http://creativecommons.org/licenses/by-nc-nd/4.0/>).

1. Introduction

The soils and vegetation of coastal wetlands, including tidal marshes, mangroves and seagrasses, represent significant long-term standing carbon (C) pools that cumulatively sequester atmospheric carbon at annual rates comparable to terrestrial forest types despite their small global coverage (McLeod et al., 2011).

* Corresponding author at: U.S. Geological Survey, Western Geographic Science Center, 345 Middlefield Road, MS-531 Menlo Park, CA 94025, USA.

E-mail addresses: kbyrd@usgs.gov (K.B. Byrd), lballanti@usgs.gov (L. Ballanti), Nathan.M.Thomas@nasa.gov (N. Thomas), dknguyen@usgs.gov (D. Nguyen), Holmquistj@si.edu (J.R. Holmquist), marc.simard@jpl.nasa.gov (M. Simard), lwindham-myers@usgs.gov (L. Windham-Myers).

These C stocks and fluxes in intertidal environments are collectively referred to as “coastal wetland blue carbon” (Pendleton et al., 2012). In particular tidal marsh C stocks sequester carbon at rates of 1–2 Mg C per hectare per year on average (IPCC, 2014), though are being converted to open water or other land cover types at rates of 1–2% globally (Bridgman et al., 2006; Duarte et al., 2005). Conversion is primarily due to increasing coastal populations, agriculture and the effects of climate change, including sea-level rise and extreme weather events (Kirwan and Megonigal, 2013; Wylie et al., 2016). Collectively, these contribute to greenhouse gas (GHG) emissions of 21–760 million Mg CO₂eq per year (Howard et al., 2017).

Given their large C stocks and high carbon sequestration rates, as well as the potential for increased GHG emissions due to human conversion and degradation, coastal wetlands have in recent years received significant attention for their potential role in climate change mitigation (Duarte et al., 2013). Entities interested in utilizing “coastal wetland blue carbon” as a management asset include voluntary C markets such as the Verified Carbon Standard (VCS). Approved VCS coastal wetland restoration and conservation projects can now receive carbon credits for reduction of GHG emissions (American Carbon Registry, 2017; Verified Carbon Standard, 2015).

In 2017 the U.S. EPA for the first time included coastal wetlands in the Agriculture Forestry and Other Land Use (AFOLU) sector of the national GHG inventory (USEPA, 2017), based on guidelines in the Intergovernmental Panel on Climate Change (IPCC) 2013 Wetlands Supplement (IPCC, 2014). Because of human use and level of regulatory oversight, all coastal wetlands in the conterminous U.S. (CONUS) were considered as managed lands similar to AFOLU guidelines for U.S. forest and cropland accounting (USEPA, 2017). As a result monitoring annual change in GHG emissions and removals within all 2.7 million Ha of CONUS tidal wetlands is now a component of annual U.S. GHG inventories. While five C pools must be reported in the inventory (soils, above- and belowground biomass, dead wood and litter), the first coastal wetlands inventory only included C stock changes for soil carbon, the largest C pool for tidal marshes, due to insufficient data on biomass, dead wood and litter. Given emergent marsh represents 80% of all CONUS tidal wetlands (U.S. Fish and Wildlife Service, 2014), its biomass can play an important role in C accounting for the coastal lands sector.

To include tidal marsh biomass in the coastal wetlands GHG Inventory, particularly at a Tier 2 level, higher temporal and spatial resolution and more disaggregated data are needed (IPCC, 2003). Information on biomass C stocks will also help to verify emission reductions for projects included in the voluntary C markets (Howard et al., 2017). Remote sensing based maps of tidal marshes, both of their extents and C stocks, can play a key role in meeting these objectives (Gonzalez et al., 2010). Remote sensing data provide a repeatable, standardized approach to assess spatial and temporal changes in biomass over large areas, fulfilling an essential component of GHG Inventories and required monitoring of carbon mitigation activities (Pettorelli et al., 2014).

In the United States the primary spatial dataset being used for tidal marsh GHG inventories is the National Oceanic and Atmospheric Administration (NOAA) Coastal Change Analysis Program (C-CAP) dataset (NOAA Office for Coastal Management, 2015), which was produced for CONUS in four to five year increments (1996, 2001, 2006, and 2010). C-CAP provides wall-to-wall Landsat-based 30-meter resolution maps of coastal lands with wetland classifications for key coastal wetland classes that include forested, scrub-shrub and emergent marsh, subdivided into palustrine (freshwater wetland with salinity less than 0.5%) and estuarine (brackish and saline wetland with salinity equal to or greater than 0.5%). Extraction of additional information on vegetation condition from the Landsat data used to derive the C-CAP maps has the potential to further characterize wetland carbon stocks.

Technical barriers to national scale remote sensing have become greatly reduced in recent years with the availability of free, post-processed satellite and aerial imagery with national to global coverage. The entire catalog of Landsat satellite images is now available georeferenced and calibrated as a surface reflectance product (Vermote et al., 2016) that can be used for biomass estimation in otherwise data scarce regions (Dube and Mutanga, 2015). Sentinel-1A and Sentinel-1B provide global, free C-band quad-pol synthetic aperture radar data approximately every 6 days. The U.S. National Agriculture Imagery Program (NAIP) offers 4-band aerial image data of the U.S. at 1 m resolution approximately every two to three years since 2003 (USDA Farm Service Agency, 2017). These datasets, along with other geophysical, climate and demographic data, are now accessible within Google Earth Engine's (GEE) platform. The GEE platform consists of a petabyte catalog of satellite imagery and geospatial datasets and a massively parallel, distributed runtime engine (Google Earth Engine Team, 2017). This combination of parallel processing and rich data archive is enabling the production of global products, such as global forest cover change maps and global surface water inundation maps (Hansen et al., 2013; Pekel et al., 2016).

Optical remote sensing of tidal marsh biomass has been performed in multiple regions, including the U.S. Southeast (Schalles et al., 2013), the Gulf of Mexico (Ghosh et al., 2016; Mishra et al., 2012), Argentina (Gonzalez Trilla et al., 2013), the U.S. Pacific Coast (Byrd et al., 2014, 2016) and South Africa (Mutanga et al., 2012) where remote sensing model error is typically below 20%. The application of radar data for tidal marsh biomass mapping has not been well tested, though it can indicate marsh dieback from hurricanes and recovery (Ramsey et al., 2014). Despite these multiple efforts, mapping is conducted using empirical models and the general assumption is that due to differences in marsh ecosystems including plant community composition, water depth and soil types, models are calibrated to specific locations and years, thus posing limitations for scaling (Lobell et al., 2015).

Tidal marsh vegetation is primarily dominated by graminoids, or grass or grass-like plants, including grasses (Poaceae), sedges (Cyperaceae), rushes (Juncaceae), and arrow-grasses (Juncaginaceae). Common genera from these families appear throughout U.S. tidal marshes, though these may vary in dominance, distribution and spatial pattern. In the U.S. Northeast and mid-Atlantic marshes, the perennial, deciduous shrub *Iva frutescens* (high-tide bush or marsh elder) can also occur. Tidal freshwater marshes are more species-rich than saline marshes though commonly include *Schoenoplectus* spp. (bulrushes), *Typha* spp. (cattail), *Polygonum* spp. (smartweed), and non-natives like *Phragmites australis* (common reed) (Vasquez et al., 2005).

One reason why empirical remote sensing models of biophysical features like biomass are not transferrable to other regions is that the differences in canopy architecture or leaf traits from one plant community to the other have different optical properties, and so generate different relationships with vegetation indices for the same level of biomass (Glenn et al., 2008; Nagler et al., 2004). For example the vertical stem morphology of many tidal marsh rushes, sedges or grasses increases light scattering and absorption in spaces between vegetation, leading to lower overall canopy reflectance (Mutanga and Skidmore, 2004; Ollinger, 2011). In contrast, the horizontal leaf angle of grass species like *Distichlis spicata* support strong relationships between biomass and vegetation indices like NDVI (Langley and Megonigal, 2012).

Given differences in leaf morphology and plant growth form among emergent marsh species, our primary objective was to generate a single remote sensing model of tidal marsh aboveground biomass and carbon that represents nationally diverse saline, brackish and freshwater marshes. In order to successfully fulfill this, we developed the first national-scale dataset of aboveground

tidal marsh biomass, species composition and aboveground plant C content from six U.S. estuaries representing a range of climate and salinity gradients. Using this dataset we test the performance of a repeatable remote sensing methodology for GHG accounting of tidal marsh aboveground C stocks that is consistent, transferable, free or low-cost and applicable to a range of estuarine characteristics.

Through the implementation of these objectives we address how the differences in plant community composition and vegetation structure across estuaries influence model development, and how additional or improved remote sensing data sets are able to improve model performance. In particular, we test the addition of Sentinel-1 C-band synthetic aperture radar backscatter with standard Landsat vegetation indices. We also explore how high resolution NAIP imagery can help to improve vegetation cover and biomass estimates. Given a final model, we evaluate uncertainties in mean aboveground C densities and total aboveground C across regions and wetland types mapped in C-CAP, and we investigate the capacity to discern regional and sub-regional differences in these estimates.

2. Methods

2.1. Site descriptions

We compiled new and existing field samples of aboveground biomass and related ancillary data from six CONUS estuaries that represent a range in climate and salinity regimes and wetland condition (Fig. 1, Table 1). These study regions include: the Cape Cod peninsula, Massachusetts; the Smithsonian Environmental Research Center Global Change Research Wetland (GCRew) on Chesapeake Bay in Anne Arundel County, Maryland; the Florida Coastal Everglades Long Term Ecological Research Site in Everglades National Park, Florida; Terrebonne and Saint Mary Parishes, Louisiana, in the Mississippi Delta; the Billy Frank Jr. Nisqually National Wildlife Refuge (NWR) in Puget Sound, Washing-

ton; and San Francisco Bay, California, which was split into two sub-regions, the saline/brackish marshes and the freshwater marshes. Images of common plant species in these regions are found in Fig. 2.

2.2. Sampling

Processing steps for the remote sensing model of tidal marsh aboveground C stocks are outlined in Fig. 3. For the first step, we compiled biomass field samples including sets of existing and newly collected data ranging from 2005 to 2015, using a sampling protocol to model biomass at the 30 m Landsat scale. In total the final published Biomass Field Plot dataset (Byrd et al., 2017) includes 2400 sample plots, with a majority from San Francisco Bay ($n = 1348$) and the Everglades ($n = 700$). Plot data include biomass measurements, species composition data and related ancillary data including water depth, thatch height and density, and percent cover live/dead vegetation, soils, open water and litter. Region specific field sampling methods are described below.

San Francisco Bay: We used existing biomass samples as described in Byrd et al. (2014) (freshwater impounded marsh, 2011–2012), Byrd et al. (2016) (brackish tidal marsh, 2014), and (Parker et al., 2012, 2011; Schile et al., 2011) (saline marsh, 2005, 2008).

Everglades: *Cladium jamaicense* aboveground live biomass has been sampled every two months at permanent plots, from 1998 to 2015 (Troxler and Childers, 2017). Allometric measurements were made in triplicate 1 m² plots at each of the sites according to Daoust and Childers (1998).

Louisiana: Biomass data and ancillary data on species composition and water depth were collected in May 2015 and at the end of August 2015. All vegetation was clipped to the ground level within a 45 cm square area, dried and weighed by species. Each site consisted of two plots positioned 5 m apart. The sites were located along transects perpendicular to the main channels.

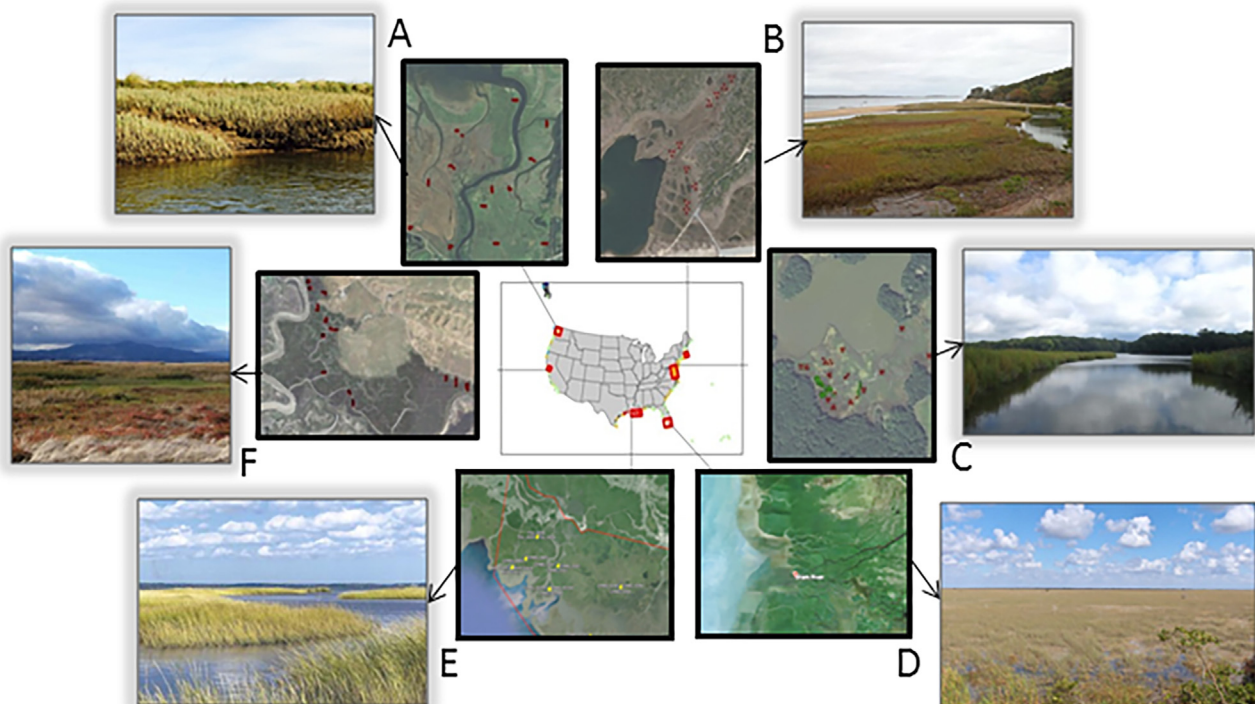


Fig. 1. Study Regions. (A) Puget Sound, Washington, Laurel Ballanti; (B) Cape Cod, Massachusetts, Lia McLaughlin; (C) Chesapeake Bay, Maryland, Grace Schwartz; (D) Everglades, Florida, paulsmithjr, CC BY-SA 3.0; (E) Mississippi River Delta, Louisiana, Greg Snedden; (F) San Francisco Bay, California, Jessica Schneider.

Table 1

Summary of environmental characteristics and climate for each site where aboveground biomass was sampled.

Region	Site Name	Latitude	Longitude	Condition	Salinity	Air Temp Avg. Max (°C)	Air Temp Avg. Min (°C)	Annual Average Precip. (mm/y)	Month of Max Precip.
Cape Cod	Waquoit Bay	41°33.406'N	70°29.776'W	NAT	S,B	14.8	5.7	1210	October
	Scusset	41°47.214'N	70°31.358'W	REST	B				
	Herring	41°56.880'N	70°3.166'W	DEG	F				
Chesapeake Bay	Global Change Research Wetland	38°53.292'N	76°33.252'W	NAT	B	17.9	7.9	1139	September
Everglades	Everglades National Park	25°22.322'N	80°52.883'W	NAT	S,B,F	30	18	1432	June
Louisiana/ Mississippi Delta	Terrebonne Parish	29°20.244'N	90°50.247'W	REST, NAT	S,B,F	26	15.6	1580	July
	St. Mary Parish	29°38.072'N	91°28.365'W	REST, NAT	S,B,F				
Puget Sound	Nisqually National Wildlife Refuge	47°5.539'N	122°42.348'W	REST, NAT	S,B	15.8	4.8	1269	November
San Francisco Bay - Brackish, Saline	Coon Island	38°11.638'N	122°19.435'W	REST	B	19.2	10.2	634	January
	Pond 2A	38°9.099'N	122°19.305'W	REST	B				
	Carl's Marsh	38°7.308'N	122°30.401'W	REST	B				
	China Camp	38°0.157'N	122°29.167'W	NAT	S				
	Rush Ranch	38°12.217'N	122°1.292'W	NAT	B				
	Bull Island	38°13.328'N	122°18.398'W	REST	B				
	Sherman Lake	38°2.414'N	121°47.788'W	DEG	B				
	Browns Island	38°2.337'N	121°51.842'W	NAT	B				
San Francisco Bay - Freshwater	Twitchell Island	38°6.578'N	121°38.914'W	REST*	F	22.9	9.8	339	January
	Mayberry Wetland	38°3.562'N	121°43.997'W	REST*	F				
	Sand Mound Slough	38°0.694'N	121°36.993'W	NAT	F				

Salinity: S = saline (30–50 parts per thousand; ppt), B = brackish (0.5–30 ppt), F = freshwater (0–0.5 ppt).

Condition: NAT = natural, REST = restored, DEG = degraded, *Impounded wetlands (obstructed water outflows).

Cape Cod, Puget Sound, and Chesapeake: Biomass samples and ancillary data were collected in these three regions during peak growing season of August–September 2015 following methods in Byrd et al. (2016). For each region, at least 30 Landsat pixel footprints were selected for sampling that represented both homogeneous pixels, in terms of species diversity and vegetation cover, and a range of Landsat NDVI values from low to high (Ghosh et al., 2016), as determined by high resolution imagery, previous summer season Landsat NDVI, and existing vegetation maps. Within each pixel footprint, three regularly spaced plots were selected for collection of biomass field samples and ancillary data, and were recorded with a sub-meter global positioning system (GPS). At each plot within 1 m * 1 m quadrats, we visually estimated percent cover of the top three dominant species as the mid-point of the Braun Blanquet cover class (Barbour et al., 1999). We sampled live aboveground biomass within a smaller quadrat nested in the 1 m * 1 m quadrats (0.5 m * 0.5 m for Cape Cod and Chesapeake, 0.5 m * 0.25 m for Puget Sound, 0.25 m * 0.25 m * 5 replicates for Chesapeake). We clipped vegetation to the ground level, separated green vegetation from dead, and then dried green vegetation at 55 °C before weighing. All biomass measurements were scaled to a square meter. At the Chesapeake site, we used allometric equations modified from Lu et al. (2016) to estimate biomass for *P. australis australis* and *I. frutescens* plants, which were sampled in 1 m² quadrats.

For each Landsat pixel footprint sampled, we identified the dominant plant species using a two-variable importance value measure, including average percent cover and frequency of occurrence among all field plots within the pixel (Barbour et al., 1999). All dominant species identified across all regions were classified by plant functional type according to height class (low: <1 m vs. high: ≥1 m), leaf inclination angle (erect, prostrate), and growth form (graminoid, forb, sub-shrub, shrub) according to the U.S. Department of Agriculture PLANTS database (USDA NRCS, 2017) and expert opinion to explore variation in plant interaction with vegetation indices and radar backscatter. Once classified, we identified only three shrub pixels, dominated by *Iva frutescens* in the Chesapeake region.

2.3. Database development

We developed a 30 m scale Biomass/Remote Sensing dataset that joins field-measured biomass values, dominant species and other ancillary information with Landsat band surface reflectance and vegetation indices, NAIP-derived fractional cover of green vegetation, and Sentinel-1 radar backscatter coefficients. The final public dataset includes 1226 Landsat pixels (Byrd et al., 2017).

Landsat Data: Using Google Earth Engine (GEE), pixels from Landsat (Landsat 5 TM, Landsat 7 ETM + and Landsat 8 OLI) surface reflectance products were matched with biomass data collected within 16 days of image acquisition (Table 2). Biomass values from plots located in the same Landsat pixel footprint were averaged, and average values were attributed to reflectance from the corresponding pixel. From surface reflectance data, we calculated all two-band vegetation indices (Thenkabail et al., 2004), the wide dynamic range vegetation index (WDRVI) (Gitelson, 2004), and the soil-adjusted vegetation index (SAVI) (Huete, 1988) (Table 3) due to their success in other remote sensing studies of marsh biomass (Byrd et al., 2016; Langley and Megonigal, 2012; Mishra et al., 2012). Major GEE processing steps are provided in Supplementary Data S1 and S2.

Blue Carbon Extent Map: The spatial extents of our aboveground carbon density maps were based on a modified 2010 C-CAP land cover dataset with estuarine or palustrine emergent marsh only. Likely non-tidal palustrine wetlands were removed from the dataset based on National Wetlands Inventory (NWI) modifiers for tidal wetland. This map was further edited to include major tidal marsh omissions such as the newly restored wetland at Nisqually NWR and tidal marsh commissions such as impounded, non-tidal wetlands in Suisun Marsh, in San Francisco Bay.

NAIP Image Classification: For each region, we generated a 1 m resolution map of tidal marsh green vegetation, non-vegetation, and open water, which was then used to calculate 30 m fractional cover of green vegetation per Landsat pixel in the Blue Carbon Extent Map. The most recent NAIP images for each region (Table 2)

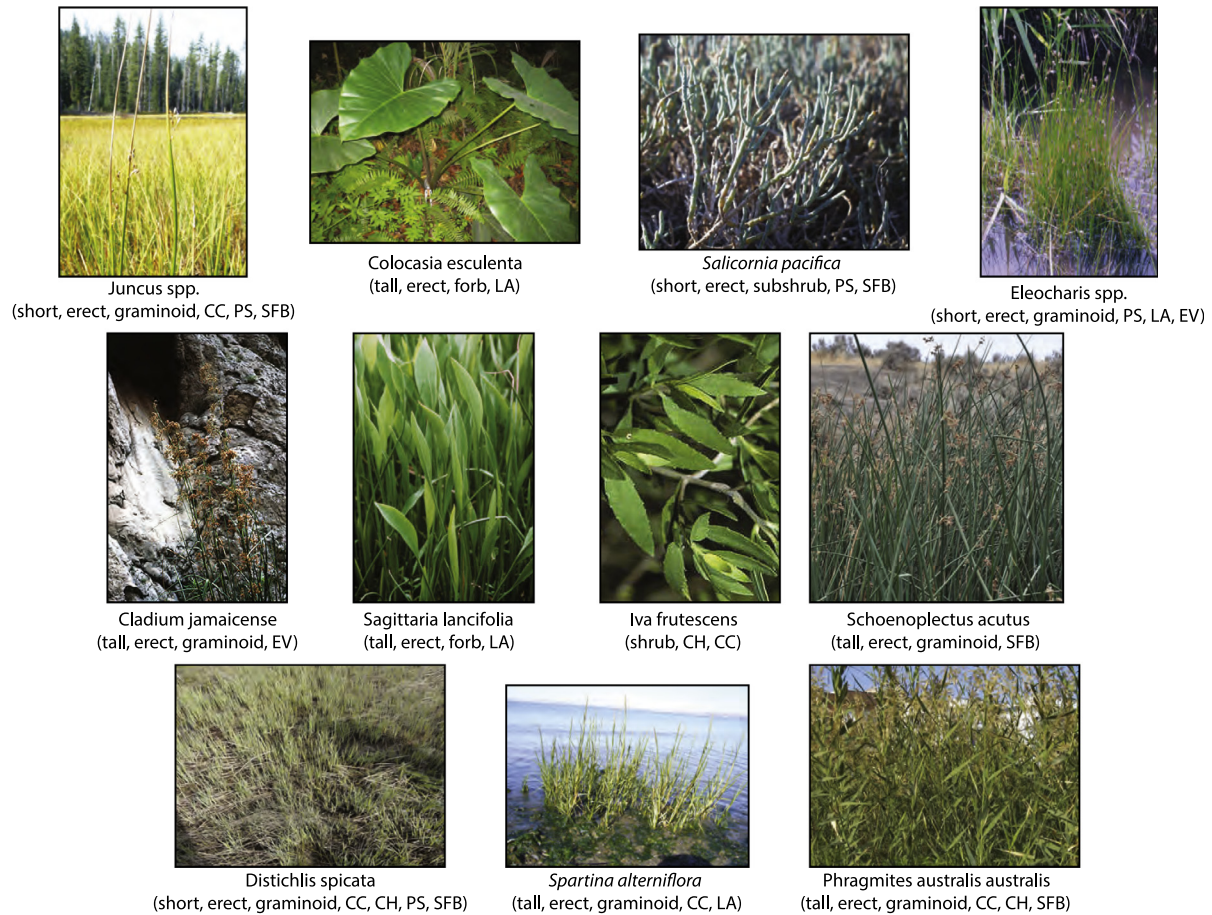


Fig. 2. Common Tidal Marsh Species, their plant functional type and region where most commonly found. *Juncus* spp., Dana York; *Colocasia esculenta*, Moorea, Biocode; *Salicornia pacifica*, Dana York; *Eleocharis* spp., Jennifer Anderson, USDA-NRCS Plants Database; *Cladium jamaicense*, Smithsonian Institute Dept. of Botany; *Sagittaria lancifolia*, George Folkerts, USDA-NRCS Plants Database; *Iva frutescens*, Robert H. Mohlenbrock, USDA-NRCS Plants Database; *Schoenoplectus acutus*, Robert Carr; *Distichlis spicata*, Laurel Ballanti; *Spartina alterniflora*, Zoya Akulova; *Phragmites australis australis*, Luigi Riganese. Region abbreviations: CC: Cape Cod, CH: Chesapeake, EV: Everglades, LA: Louisiana, SFB: San Francisco Bay, PS: Puget Sound.

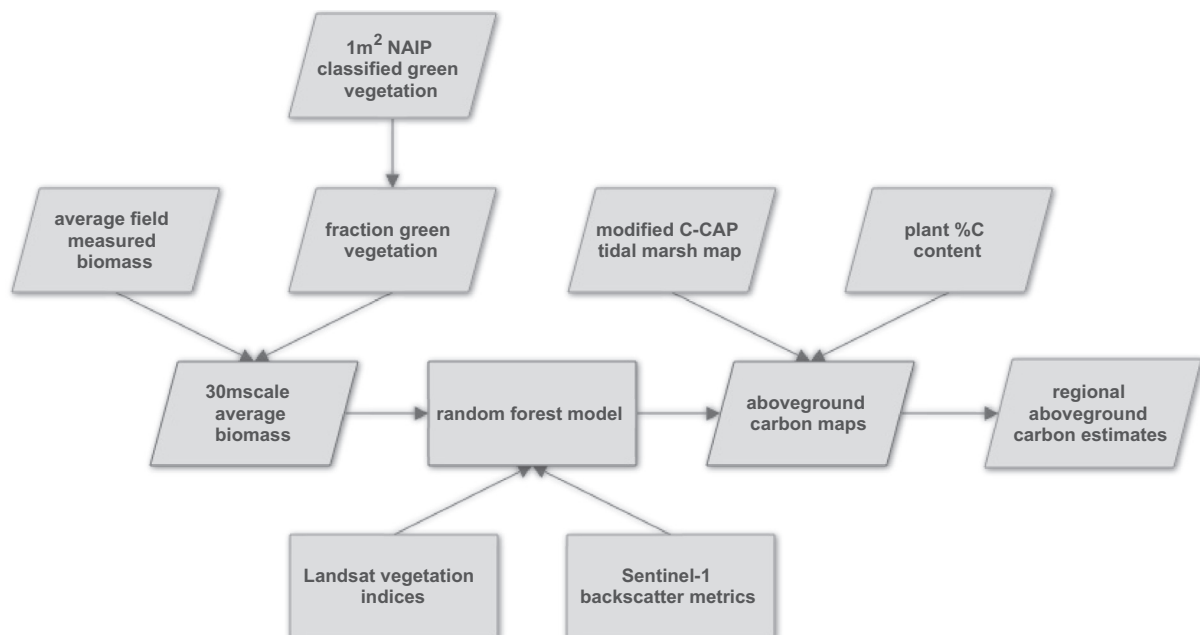


Fig. 3. Flowchart of processing steps.

Table 2
Dates of field data collection and image acquisition. Field data were matched with Landsat data acquired within 16 days and with Sentinel-1A data acquired within 30 days of field data collection.

Region	Field data	Landsat ETM+	Landsat OLI	Sentinel-1A	NAIP
Cape Cod	8/10/2015–9/16/2015		8/5/2015, 9/6/2015	8/16/2015	07/13/2014, 7/18/2014, 7/29/2014
Chesapeake	9/1/2015–9/28/2015		8/17/2015, 9/18/2015	8/25/2015	8/1/2014, 8/14/2015, 8/15/2015, 9/07/2013, 9/25/2013
Everglades	7/28/1999–8/27/2015 ^a	1999–2015 ^a	2013–2015 ^a	9/21/2015	10/11/2013, 10/12/2013, 10/18/2013, 10/19/2013, 10/27/2013–10/29/2013, 11/3/2013, 11/4/2013, 11/28/2013, 12/6/2013, 12/18/2013
Louisiana	5/6/2015–10/2/2015	5/6/2015, 8/26/2015	5/5/2015, 8/23/2015, 8/25/2015, 10/5/2015, 10/12/2015	8/18/2015	3/30/2015, 8/26/2015–8/27/2015
Puget Sound	8/4/2015–8/27/2015		8/1/2015, 8/17/2015	8/11/2015	7/30/2015, 8/25/2015
San Francisco Bay	2005, 2007, 2008, 2011–2012, 2014 ^a	2005–2012 ^a	5/21/2014, 6/6/2014, 6/22/2014, 7/8/2014, 7/24/2014, 8/9/2014		6/6/2014, 6/8/2014, 6/21/2014, 6/28/2014

^a See Byrd et al. (2017) for specific field and image dates.

Table 3
Remote sensing-based variables tested in random forest models.

Landsat ETM+, OLI (30 m)
Two-band vegetation indices: $TBVI_{ij} = (R_j - R_i)/(R_j + R_i)$
Wide dynamic range vegetation index:
$WDRVI2 = (0.2 * NIR - R)/(0.2 * NIR + R)$
$WDRVI5 = (0.5 * NIR - R)/(0.5 * NIR + R)$
Soil adjusted vegetation index: $SAVI = (NIR - R) * 1.5 / (NIR + R + 0.5)$
Sentinel-1 C-band SAR (10 m)
VH, VV mean backscatter coefficient in green segment of Landsat pixel
VH, VV backscatter standard deviation in green segment of Landsat pixel
VH, VV backscatter coefficient of variation in green segment of Landsat pixel
National Agriculture Imagery Program images (1m)
Fraction green vegetation in Landsat pixel

[‡]NIR = near infrared reflectance.

[§]R = red reflectance.

[†] R_i and R_j are the reflectance values in bands i and j.

were downloaded for free from earthexplorer.usgs.gov and mosaicked in ERDAS Imagine MosaicPro using the color balance correction. The NAIP classification was performed in eCognition, which applies an object oriented approach, beginning with the multi-resolution segmentation tool to isolate spectrally similar pixels as objects. Object oriented-analysis has shown higher accuracy and removal of speckle noise in high resolution imagery such as NAIP, compared to pixel-based analysis (Li and Shao, 2014; Yuan and Bauer, 2006). Parameters for shape and compactness were set to the default values of 0.1 and 0.5, and the scale parameter, which determines segmentation size, was set by region based on trial and error. Once the segmentation was complete, the objects were classified using spectral thresholds based on the 4 NAIP bands, NDVI, the Normalized Difference Water Index (NDWI) (McFeeters, 1996) and mean brightness. We calculated the percent of each class within Landsat pixel extents, and generated 30 m resolution maps of fraction green vegetation for each region. We conducted an accuracy assessment of the NAIP classification by selecting 150 random points within each region. Each sample point was assigned to a class based on visual interpretation of the NAIP imagery (Supplementary Data S3).

Sentinel-1 Data: Sentinel-1 data collected from August 11 to September 21, 2015 (Table 2), were acquired from the European Space Agency (ESA) via the Copernicus Open Access Hub (<https://scihub.copernicus.eu/>). Cross-polarized data were not available at all locations, in which case we used co-polarized imagery. The raw data were pre-processed via the ESA Science Toolbox Exploration Platform (STEP). The data were calibrated for radiometric and geometric effects and filtered to remove speckle noise using the Lee (1981) algorithm. We calculated several variables for both

the vertical transmit and vertical receive (VV) and vertical transmit and horizontal receive (VH) polarizations, including mean backscatter coefficient, backscatter standard deviation, backscatter coefficient of variation (i.e. standard deviation over mean amplitude) for the whole Landsat pixel and for the green segment of the pixel calculated from the 1 m map of green vegetation cover. Backscatter variables were only matched with biomass field data collected within one month of image acquisition (Byrd et al., 2017).

2.4. Biomass modeling – random forest

For modeling purposes, we retained samples in the Biomass/Remote Sensing dataset if biomass could be matched with Landsat 8 or Landsat 7 surface reflectance data; given that Landsat 8 OLI NDVI is greater than Landsat 7 ETM + NDVI due to different spectral response functions between the sensors, we applied a surface reflectance sensor transformation function to all Landsat 7 band surface reflectance values to transform them to Landsat 8 surface reflectance (Roy et al., 2016). Transformation functions do not exist between Landsat 8 and Landsat 5; therefore samples matched with Landsat 5 were not used. Landsat 5 samples were only located in the Everglades or San Francisco Bay. Given the disproportionately greater sample number in these regions ($n > 500$ each) compared to other regions ($n < 50$ each), we selected a stratified random sample of pixels in the Everglades and both San Francisco Bay sub-regions (salt/brackish and freshwater) while maintaining biomass distributions. The final national scale dataset for the modeling exercise had a sample number of 409 30 m resolution pixels.

We built empirical biomass models from the full national scale dataset using a random forest machine learning algorithm in the R caret package, using the “ranger” model. Random forest (Breiman, 2001) is a non-parametric classification and regression tree approach that uses ensembles (forests) of classification or regression trees, with each tree selecting and permuting randomized subsets of predictor variables. The iteration and randomization procedure accommodates non-linear responses, categorical or continuous variables, and missing values, it can manage complex interactions among variables, and has been useful for building remote sensing biomass and productivity models (Gonzalez-Roglich and Swenson, 2016; Greaves et al., 2016; Tramontana et al., 2015). The ranger model, which generates 500 trees per model run, allows for tuning of the “mtry” parameter, which determines the number of variables randomly tested for a split at each tree node.

From all generated Sentinel-1 and Landsat variables, we removed those collinear variables from the model where Pearson’s correlation coefficient > 0.80 . We retained variables in the model

with high variable importance measures that contributed to an improved model fit, as indicated by a reduction in root mean square error (RMSE). The permutation variable importance measure – also referred to as the mean decrease in accuracy – reflects the average change in mean square error normalized by the standard error after permuting a variable (Kuhn, 2008), and has been used to select the most relevant remote sensing model variables (Belgiu and Drăguț, 2016).

Model training was based on a 10-fold cross validation resampling method repeated 5 times, which generates test predictions for all samples, allowing exploratory data analysis of cross-validated predictions and independent variables. With a 10-fold cross validation repeated 5 times, the model is fit 50 times, and the operation generates 50 RMSE values, which can be used to generate a mean RMSE and its confidence intervals. Models were evaluated by RMSE, RMSE confidence intervals from final predictions (Byrd et al., 2014), percent normalized RMSE [RMSE/(max observed – min observed)] and the mean RMSE \pm confidence intervals from the 50 cross-validation model runs.

Models were built with non-correlated Landsat vegetation indices and Sentinel-1 radar backscatter variables, and a factor variable for region, which was included to explore the role of site effects in predicting biomass values nationally. The dependent variable was average field-measured biomass per Landsat pixel, scaled by fraction vegetation cover in the pixel (biomass * FVC) (Byrd et al., 2016). Model sets are listed in Table 6. With Sentinel-1 data only available for four of the seven regions, we built a national-scale Landsat-only random forest model that included samples from all regions. Four national-scale models were tested and compared: (1) the full Landsat model, (2) the full Landsat model, without the three *I. frutescens* shrub plots, (3) the full Landsat model, without the three *I. frutescens* shrub plots, using average unscaled field measured biomass as the dependent variable, and (4) the full Landsat model, without the three *I. frutescens* shrub plots, and without the “site” factor variable. Models with both Landsat and Sentinel-1 variables were generated with data subsets representing the regions where Sentinel-1 data were available.

Using cross validated predictions from the final model, we evaluated model bias by regressing observed vs. predicted values, and compared slope and intercept parameters against the 1:1 line (Piñeiro et al., 2008). We also plotted predicted biomass vs. independent variables with the highest importance measures.

2.5. Aboveground carbon density maps

We selected the best performing random forest model as determined by RMSE, percent normalized RMSE, and dynamic range of predicted values. Based on this final model and Landsat images collected during August 2015, when peak biomass typically occurs, we generated aboveground biomass predictions for the Blue Carbon Extent Maps.

Percent C in aboveground plant tissue (dry weight biomass) was determined by compiling existing data from three regions of the U.

S.: the San Francisco Bay-Delta, Puget Sound, and the GCREW site in Chesapeake Bay [Byrd, 2012, unpublished data; (Janousek et al., 2017), P. Megonigal, unpublished data, personal communication 5/10/2017]. Mean %C was used to convert biomass predictions to aboveground C densities to generate regional maps of tidal marsh aboveground C.

2.6. Uncertainty in regional aboveground carbon stocks

Applying the aboveground C density maps, mean aboveground C densities (Mg/ha) and total aboveground C stocks (Mg) were reported for each C-CAP wetland type (estuarine emergent and palustrine emergent) for each region, and their uncertainties.

To propagate uncertainties (standard errors) in mean C density and total C, we applied the multivariate delta method, which provides approximate variance estimates when sample sizes are large (Ver Hoef, 2012), and has been used in past carbon stock assessments (Goidts et al., 2009; Magnussen et al., 2014). Given x = mean biomass (Mg/ha), y = proportion of plant aboveground C relative to biomass, and z = map area (ha), when the metrics are independent, then the variance approximations are:

$$\text{Var}(xy) \approx y^2\text{Var}(x) + x^2\text{Var}(y) \quad (1)$$

$$\text{Var}(xyz) \approx (yz)^2\text{Var}(x) + (xz)^2\text{Var}(y) + (xy)^2\text{Var}(z) \quad (2)$$

where $\text{Var}(x)$, $\text{Var}(y)$, and $\text{Var}(z)$ might be approximated as the square of the standard errors for the measurements x , y , and z , respectively. After calculating these variance estimates, then standard errors for xy and xyz are calculated by taking $\sqrt{\text{Var}(xy)}$ and $\sqrt{\text{Var}(xyz)}$.

Standard error for mean biomass per region and wetland type was calculated through error propagation of the standard error of predicted biomass and model random error. To calculate standard error of estimated C-CAP map area, we applied methods in Olofsson et al. (2014) for calculating unbiased area estimates and confidence intervals for land cover classes based on the national 2010 C-CAP accuracy assessment published in McCombs et al. (2016). The C-CAP confusion matrix was used to calculate proportional areas for all 22 C-CAP classes. Then for the mapped estuarine emergent and palustrine emergent areas in each study region we calculated a ratio of estimated area to mapped area and their standard errors.

3. Results

3.1. Field sample results

Live aboveground green biomass field samples, averaged to the 30 m Landsat pixel area, averaged 501 g/m² nationally ($n = 409$, C. I. = 450–552 g/m²) (Table 4). While the maximum measured value at the 30 m scale was 3124 g/m², located in the San Francisco Bay-Delta freshwater marshes, 95% of the samples at the 30 m scale were 1560 g/m² or less. Values above 2000 g/m² were found in the Chesapeake site, associated with *Iva frutescens*, and the San

Table 4
Summary statistics for measured aboveground live biomass averaged by Landsat pixel for each region, in g/m².

Estuary	N	Mean	Std. Err.	[95% Conf.	Interval]	min	max
Cape Cod	33	706	67	568	843	206	1767
Chesapeake	23	1141	157	817	1466	120	2807
Everglades	87	147	16	114	179	0	602
Louisiana	29	637	67	499	774	207	1833
Puget Sound	38	447	36	375	519	51	919
SFBay-B/S	99	410	25	361	459	78	1559
SFBay-FW	100	664	75	515	813	14	3124
Total	409	501	26	450	552	0	3124

Francisco Bay freshwater sites, associated with *Typha* spp. and *Schoenoplectus acutus*.

3.2. Tidal marsh plant functional types

Tall, erect, graminoids were the most common plant type, representing 277 samples out of 409 used for model development. This plant functional type was most common in five of the seven regions,

with the exception of Puget Sound (dominated by short, erect, graminoids) and Louisiana (dominated by tall, erect, forbs). Thirty-eight samples were classified as forb-dominated. *Salicornia pacifica*, classified as a sub-shrub due to its woody stems, dominated 46 samples on the West Coast. Across regions, the species and genera most frequently classified as dominant were *Distichlis spicata* (3 regions), *Phragmites australis australis* (3 regions), *Spartina* spp. (4 regions), *Schoenoplectus* spp. (3 regions), and *Typha* spp. (4 regions) (Table 5).

Table 5

Dominant species within each Landsat pixel sample according to importance value, classified by plant functional type, within each region.

Dominant species, by plant type	Cape Cod	Chesapeake	Everglades	Louisiana	Puget Sound	SFBay-B/S	SFBay-FW
Short, erect, graminoid							
<i>Agrostis stolonifera</i>					1		
<i>Carex lyngbyei</i>					1		
<i>Distichlis spicata</i>	5	1			17		
<i>Eleocharis acicularis</i>					1		
<i>Eleocharis montana</i>				1			
<i>Eleocharis</i> sp.				2			
<i>Juncus gerardii</i>	1						
<i>Scirpus cernuus</i>					4		
<i>Spartina patens</i>		8					
<i>Triglochin maritima</i>					1		
Sub-Total	6	9	0	3	25	0	0
Tall, erect, graminoid							
<i>Bolboschoenus maritimus</i>					1	14	
<i>Cladium jamaicense</i>			87				
<i>Phalaris arundinacea</i>					1		
<i>Phragmites australis australis</i>	7	9					2
<i>Schoenoplectus acutus</i>						9	19
<i>Schoenoplectus americanus</i>		2				12	19
<i>Schoenoplectus californicus</i>						2	3
<i>Spartina alterniflora</i>	15			6			
<i>Spartina foliosa</i>						7	
<i>Typha angustifolia</i>						4	17
<i>Typha domingensis</i>				1		2	8
<i>Typha latifolia</i>	5						
<i>Typha</i> sp.				2		2	21
Sub-Total	27	11	87	9	2	52	89
Short, prostrate, forb							
<i>Alternanthera philoxeroides</i>				1			
<i>Ludwigia grandiflora</i>				1			
<i>Ludwigia peploides</i>							2
<i>Ludwigia uruguayensis</i>				1			
<i>Lysimachia maritima</i>					1		
<i>Potentilla anserina</i>							1
<i>Ranunculus repens</i>					1		
Sub-Total	0	0	0	3	2	0	3
Short, erect, forb							
<i>Cotula coronopifolia</i>					3		
<i>Polygonum punctatum</i>				1			
<i>Salicornia europaea</i>						2	
<i>Salsola soda</i>						1	
<i>Symphyotrichum subspicatum</i>					1		
Sub-Total	0	0	0	1	4	3	0
Tall, erect, forb							
<i>Colocasia esculenta</i>				8			
<i>Helenium bigelovii</i>							5
<i>Lepidium latifolium</i>						2	
<i>Sagittaria lancifolia</i>				4			
<i>Sparganium eurycarpum</i> spp. <i>eurycarpum</i>							1
Sub-Total	0	0	0	12	0	2	6
Tall, prostrate, forb							
<i>Rumex californicus</i>							2
Sub-Total	0	0	0	0	0	0	2
Short, erect, sub-shrub							
<i>Salicornia pacifica</i>					5	41	
Sub-Total	0	0	0	0	5	41	0
Tall, erect, shrub							
<i>Iva frutescens</i>		3					
Sub-Total	0	3	0	0	0	0	0
TOTAL	33	23	87	28	38	98	100

3.3. NAIP classification

Overall accuracy for the regional NAIP classifications ranged from 80.5% to 98%. Producer's accuracy and user's accuracy for green vegetation exceeded 90% for Cape Cod, San Francisco Bay, Chesapeake, and Louisiana (Supplementary Data S3). Resulting high resolution maps of fraction green vegetation show distinct trends across regions, for example the Louisiana region, with vegetation cover lower in the southeast Terrebonne Parish (Fig. 4).

3.4. Random forest biomass modeling

All national-scale Landsat models contained the same six Landsat vegetation indices as independent variables (Table 6). Model #2, using scaled biomass as the dependent variable and removing the shrub plots, performed the best, with an RMSE of 310 g/m² and a percent normalized RMSE of 10.3% (Fig. 5). Regression of observed vs. cross-validation predictions did not indicate presence of model bias. The intercept of the regression was not significantly different than 0 (p -value = 0.258), and the slope was not significantly different than 1 (p -value = 0.493). However model error was not significantly less than those of the other models, as indicated by two metrics – the confidence intervals around the final model RMSEs (Table 6) and the confidence intervals around each mean RMSE generated from the 50 cross-validation training/test sets (Fig. 6).

For both the full Landsat model and the Landsat model minus *I. frutescens*, SAVI had the highest importance score, followed by the red/green NDVI-type index and WDRVI5 (Table 7). Removing the shrub samples from the model drops the importance score of “Chesapeake” from 41.4 to 18.7, and all site variables were ranked lower in importance than all Landsat vegetation indices.

Interpretation of random forest variable dependence plots (predicted values vs. variables) and associated trend lines can only be in general terms, as predictions are a function of all variables in the model (Ehrlinger, 2015). Trend lines in predicted biomass vs. SAVI follow a quadratic form, and diverge by region and plant

growth form (graminoid or forb), with forbs being most common in the Louisiana region (Fig. 7.)

In the combined Landsat/Sentinel-1 VH and VV band model, the VH backscatter coefficient of variation had the highest importance value of all radar variables (Table 7). While this variable did not significantly improve model outcomes, it does show an association with predicted biomass values (Fig. 8). Given CV = Standard deviation/Mean, Fig. 8 shows positive associations between predicted biomass and both mean backscatter coefficient and backscatter standard deviation for each of the three regions, Chesapeake, Everglades, and Louisiana, where both VH and VV band data were available. Within Chesapeake samples, the highest predicted values are represented by *I. frutescens* plots (tall, erect, shrub) and *P. australis* (tall, erect, graminoid).

3.5. Regional aboveground carbon density maps

From a compilation of existing %C data for leaf and stem tissues of tidal marsh emergent vegetation across the U.S., the average %C value was 44.1%, with standard error of $\pm 0.064\%$ ($n = 1384$; C.I. = 43.99%–44.24%; median = 44.37%). Biomass predictions were generated for our study regions according to model #2 (Table 6), which excludes *I. frutescens* shrub plots and is calibrated on average biomass within the Landsat pixel (average field measured biomass * fraction green vegetation in the pixel). After converting biomass values to carbon densities, maps were generated for the Blue Carbon extent map (Fig. 9). Maps do not include scrub-shrub or forested C-CAP wetland classes. Maps reveal trends in aboveground carbon within and across regions. The Chesapeake Bay marshes include vegetation with C density > 4 Mg/ha more frequently than other regions. The southeastern end of Louisiana (Terrebonne Parish) contains C densities below 1 Mg/ha, though higher C (>4 Mg/ha) is present on the prograding Atchafalaya Delta (St. Mary Parish). In San Francisco Bay, moving from west to east and further inland from open bay waters, a gradient of low to high carbon matches the high to low salinity gradient there.

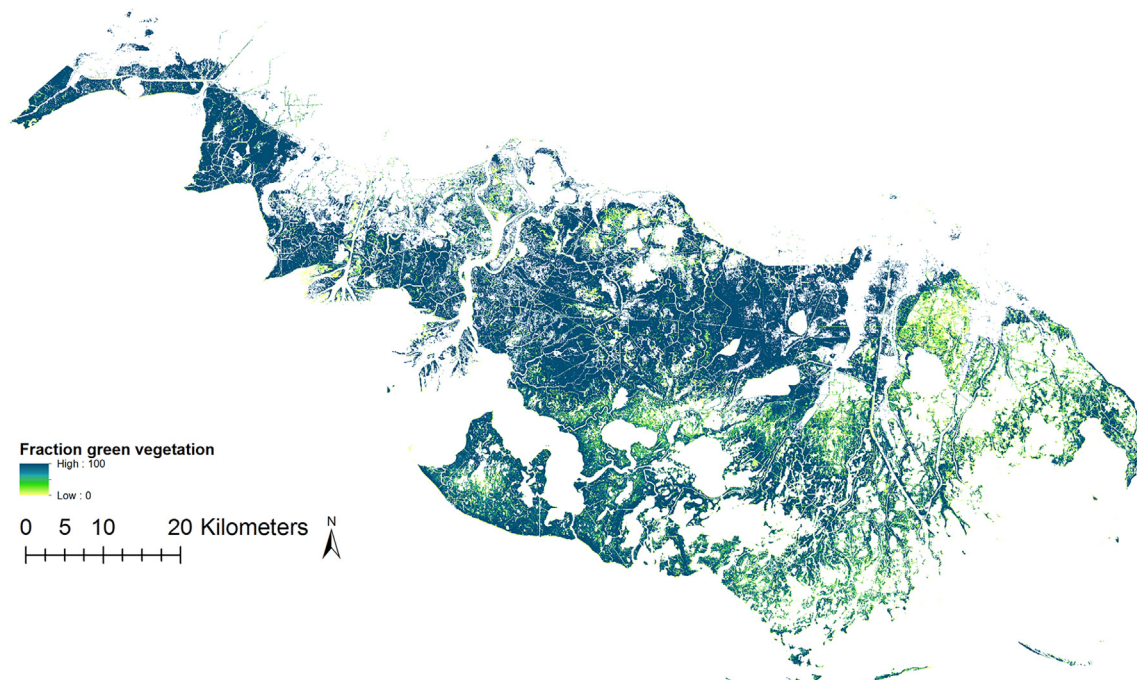


Fig. 4. Fraction green vegetation per 30 m Landsat pixel for Terrebonne and St. Mary Parishes, Louisiana, as classified in 1 m National Agriculture Imagery Program 2015 images.

Table 6

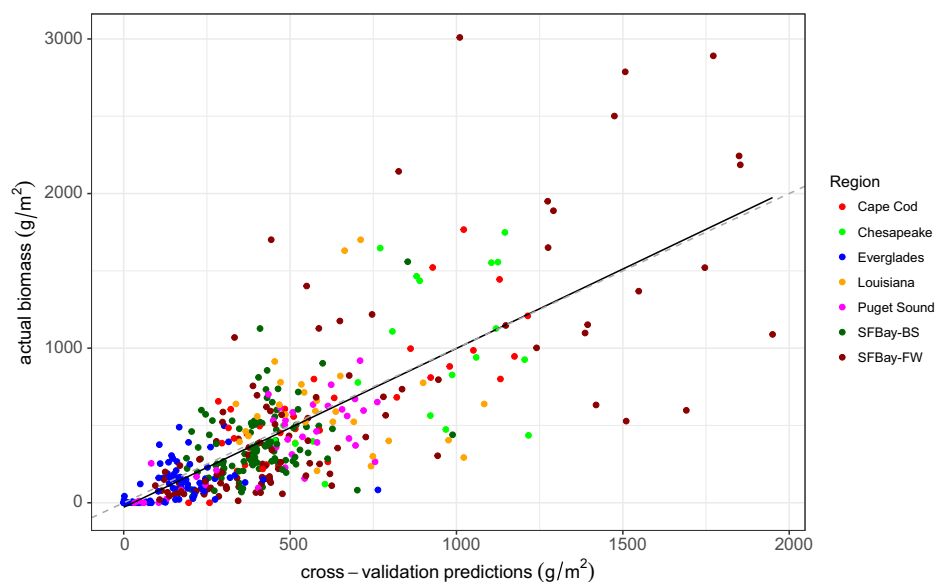
Random forest model results; Dependent variable is average aboveground green biomass at 30 m.

Datasets	Variables	#Sites	N	RMSE \pm C.I. (g/m ²)	% NRMSE	R ²
Landsat – full model	SAVI, nd_r_g, WDRVI5, nd_g_b, nd_swir2_r, nd_swir2_nir, site	6	409	327 \pm 44	11%	0.59
Landsat minus <i>Iva frutescens</i> plots	SAVI, nd_r_g, WDRVI5, nd_g_b, nd_swir2_r, nd_swir2_nir, site	6	406	310 \pm 42	10.3%	0.58
Landsat, minus <i>Iva frutescens</i> plots; dep. var: unscaled avg. biomass	SAVI, nd_r_g, WDRVI5, nd_g_b, nd_swir2_r, nd_swir2_nir, site	6	406	329 \pm 44	11%	0.56
Landsat, minus <i>Iva frutescens</i> plots, no site variable	SAVI, nd_r_g, WDRVI5, nd_g_b, nd_swir2_r, nd_swir2_nir, site	6	406	330 \pm 44	11%	0.52
Landsat plus VV band dataset	SAVI, nd_r_g, WDRVI5, nd_g_b, nd_swir2_r, nd_swir2_nir, sentvvGrCV, site	4	89	369 \pm 107	13.4%	0.63
Landsat plus VV band dataset, minus VV band variables	SAVI, nd_r_g, WDRVI5, nd_g_b, nd_swir2_r, nd_swir2_nir, site	4	89	363 \pm 107	13.3%	0.63
Landsat plus VV band dataset, minus Landsat variables	sentvvGrCV, site	4	89	448 \pm 145	16.3%	0.48
Landsat plus VH band dataset	SAVI, WDRVI5, nd_g_b, nd_swir2_r, sentvhGrSTD, site	4	86	408 \pm 121	15.3%	0.56
Landsat plus VH band dataset, minus VH band variables	SAVI, WDRVI5, nd_g_b, nd_swir2_r, site	4	86	401 \pm 120	14%	0.58
Landsat plus VH band dataset, minus Landsat variables	SAVI, WDRVI5, nd_g_b, nd_swir2_r, sentvhGrSTD, site	4	86	479 \pm 173	18%	0.36
Landsat plus VV band and VH band dataset	SAVI, WDRVI5, nd_g_b, nd_swir2_r, sentvhGrCV, sentvvGrCV, site	3	56	473 \pm 170	17.6%	0.58
Landsat plus VV band and VH band dataset, minus VV band variable	SAVI, WDRVI5, nd_g_b, nd_swir2_r, sentvhGrCV, site	3	56	474 \pm 179	18.1%	0.59
Landsat plus VV band and VH band dataset, minus VH band variable	SAVI, WDRVI5, nd_g_b, nd_swir2_r, sentvvGrCV, site	3	56	463 \pm 174	17.6%	0.60
Landsat plus VV band and VH band dataset, minus VH and VV band variables	SAVI, WDRVI5, nd_g_b, nd_swir2_r, site	3	56	459 \pm 171	17.2%	0.60
Landsat plus VV band and VH band dataset, minus Landsat variables	sentvhGrCV, sentvvGrCV, site	3	56	537 \pm 206	20.4%	0.47
Landsat plus VV band and VH band dataset, minus <i>Iva frutescens</i> plots	SAVI, WDRVI5, nd_g_b, nd_swir2_r, sentvhGrCV, sentvvGrCV, site	3	53	366 \pm 140	22.4%	0.60
Landsat plus VV band and VH band dataset, minus <i>Iva frutescens</i> plots, VV or VH band	SAVI, WDRVI5, nd_g_b, nd_swir2_r	3	53	361 \pm 139	21.8%	0.61

VV band: in Chesapeake, Everglades, Louisiana, Puget Sound; VH band: in Cape Cod, Chesapeake, Everglades, Louisiana.

SAVI = soil adjusted vegetation index; WDRVI5 = wide dynamic range vegetation index; nd_r_g = normalized difference green/blue index; nd_swir2_r = normalized difference swir2/red index; nd_r_g = normalized difference red/green index; nd_swir2_nir = normalized difference swir2/nir index.

sentvvGrSTD = VV band backscatter std.dev in green segment; sentvvGrCV = VV band backscatter coefficient of variation in green segment; sentvhGrCV = VH band backscatter coefficient of variation in green segment.

**Fig. 5.** Cross-validation predictions vs. observed average aboveground green biomass at 30 m for final biomass model (model #2, table 6; n = 406, RMSE = 310 g/m²). Solid black line = linear fit of actual and predicted values; dotted gray line = 1:1 line.

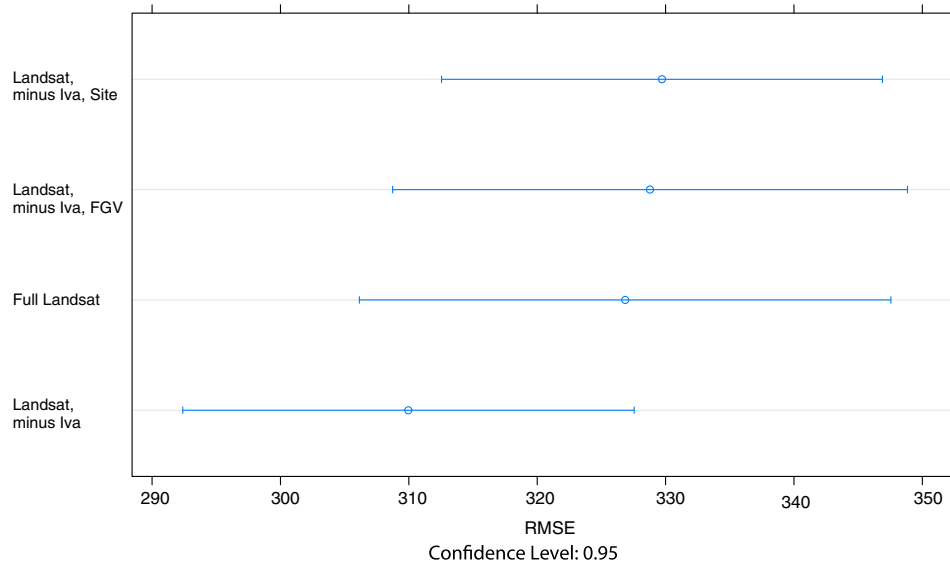


Fig. 6. Comparison of four national-scale Landsat models. Dotplot shows average RMSE and confidence intervals from 50 cross-validation test samples. (1) Landsat, minus Iva, Site = model without *I. frutescens* samples, site variable; (2) Landsat, minus Iva, FGV = model without *I. frutescens* samples, and with unscaled biomass; (3) Full Landsat = full model; (4) Landsat, minus Iva = model without *I. frutescens* samples, and with biomass scaled by fraction green vegetation.

Table 7

Random forest scaled variable importance scores for each variable for a subset of models in Table 6. Model number is in parentheses.

Landsat-Full Model (#1)	Importance Score	Landsat – minus <i>I. frutescens</i> (#2)	Importance Score	Landsat + Sentinel VV, VH bands (#11)	Importance Score
SAVI	100.0	SAVI	100.0	nd_swir2_r	100.0
nd_r_g	72.6	nd_r_g	69.4	SAVI	91.3
WDRVI5	67.5	WDRVI5	57.5	WDRVI5	87.3
Chesapeake	41.4	nd_g_b	35.1	sentvhGrCV	51.2
nd_g_b	37.9	nd_swir2_r	34.4	Chesapeake	51.0
nd_swir2_r	36.5	nd_swir2_nir	24.4	nd_g_b	48.0
nd_swir2_nir	23.6	Chesapeake	18.7	Everglades	40.9
Everglades	4.9	Everglades	6.9	sentvvGrCV	39.3
SFBay-FW	4.7	SFBay-FW	5.6	Louisiana	14.7
SFBay-B/S	4.5	SFBay-B/S	3.4		
Louisiana	0.8	Louisiana	0.8		
Puget Sound	0.0	Puget Sound	0.0		

3.6. Uncertainty in aboveground carbon stocks

Due to the large number of pixels per region, mean aboveground C standard error was very low. Error in total aboveground C was mainly influenced by error in estimated map area. The largest present day carbon pools were found in the Terrebonne and St. Mary Parishes, LA at 507,761 Mg (S.E. \pm 14,822 Mg) (Table 8). Given the small, fragmented coverage of freshwater tidal wetlands in the San Francisco Bay region, aboveground biomass carbon pools totaled 5190 Mg (S.E. \pm 231 Mg). Mean carbon densities ranged from 0.97 Mg/ha (S.E. \pm 0.003 Mg/ha) in palustrine emergent Everglades marshes, to 2.67 Mg/ha (S.E. \pm 0.004 Mg/ha) in palustrine emergent Louisiana marshes.

4. Discussion

This study represents the first time that a U.S. national-scale remote sensing model of tidal marsh aboveground C stocks has been produced. This modeling effort was made feasible by compiling the first nationwide dataset ($n = 2400$ samples) of aboveground live biomass of emergent marsh from six regions representing the conterminous U.S. Pacific, Atlantic, and Gulf coasts. The random forest model, driven by six Landsat vegetation indices, had an

RMSE of 310 g/m², or slightly over 10% normalized RMSE. This model captured variation in plant community composition, soil types, and background effects such as plant litter and surface water, thus greatly reducing the scaling limitations of models calibrated to specific locations (Lobell et al., 2015). Also this research represents the first time national data on percent carbon in emergent marsh plant tissue has been synthesized, illustrating a narrow range for %C in tidal marsh plant tissues (C.I.: 43.99%–44.24% per gram dry weight). Combined with spatially explicit biomass estimates, this narrow distribution provides a method to improve estimates for aboveground C stocks in tidal marshes, the coastal wetland blue carbon ecosystem with the greatest areal coverage in the conterminous U.S. This modeling and data synthesis effort will allow for aboveground C stocks in tidal marshes to be included in the coastal wetland section of the U.S. National Greenhouse Gas Inventory.

While the random forest model does not provide a spatially explicit assessment of accuracy, it ultimately accounts for variability in remote sensing (e.g. Landsat reflectance and radar backscatter), *in situ* measurements and spatial and temporal plot collocation errors. Relatively low model error may be attributed to overall similarities in tidal marsh plant functional type across regions (Table 5; erect graminoids represented 36–100% of sam-

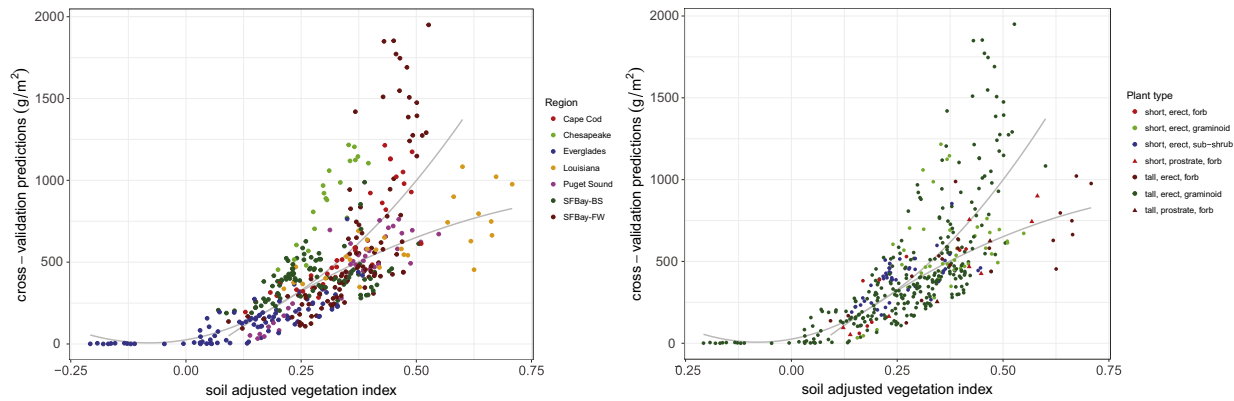


Fig. 7. Cross-validated biomass predictions vs. soil adjusted vegetation index (SAVI) values for final biomass model (model #2, table 6; $n = 406$, $RMSE = 310 \text{ g/m}^2$). Samples classified by a) region and b) plant functional type. Plots indicate different quadratic trend lines between predictions and SAVI for two main plant growth forms, graminoid ($537 * SAVI + 2735 * SAVI^2 + 26$; $R^2 = 0.54$, $n = 368$) and forb, which is most common in Louisiana ($2082 * SAVI - 1021 * SAVI^2 - 134$; $R^2 = 0.69$, $n = 38$).

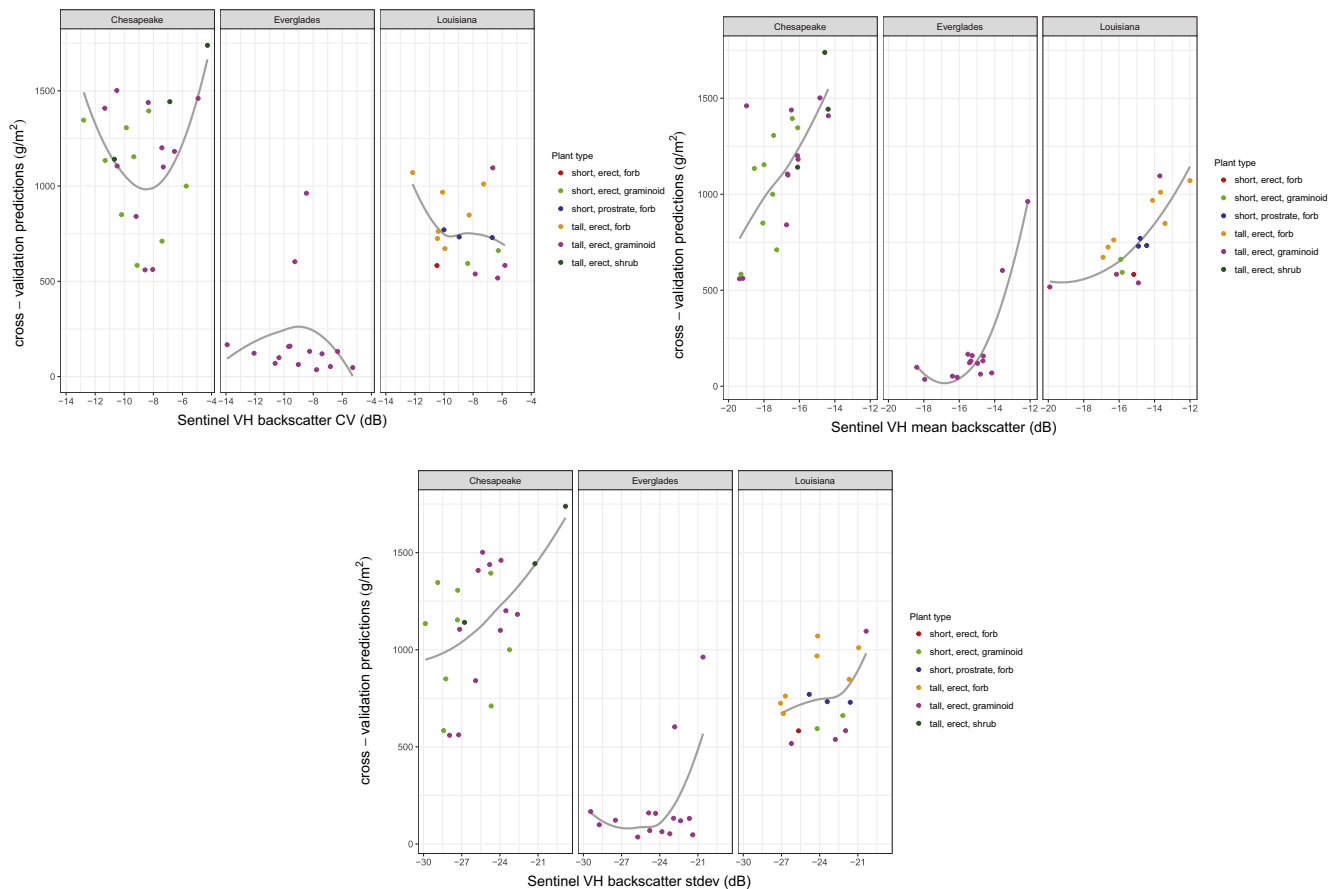


Fig. 8. Sentinel-1 VH band (a) backscatter coefficient of variation, (b) mean backscatter coefficient and (c) backscatter standard deviation plotted against cross-validation biomass predictions for model (#11) (Table 6), by region. Samples are classified by plant functional type.

ples in each region), but also to the random forest algorithm, which partitions samples into similar groups via permutation of predictor variables in the generation of regression tree ensembles. Variation in leaf and canopy properties across functional types influences retrieval of reflectance and biomass estimation with remote sensing (Shoko et al., 2016). Although plant functional type was not a variable in the model, Fig. 7 suggests that the random forest algorithm partitioned samples according to plant type, particularly growth form, when generating predictions, thereby handling the variation in retrieval of reflectance across samples. These patterns reflect commonly understood leaf optical properties, that broadleaf

plants typically exhibit a higher reflectance in the NIR region of the spectrum, compared to plants characterized by narrow leaf, vertical stems.

The random forest variable importance measurement was used to select the optimal variables for the biomass models (Belgiu and Drăguț, 2016). The full national Landsat model was developed with six common vegetation indices – the SAVI, the Red/Green TBVI, the WDRVI5, The SWIR-2/Red TBVI, the Green/Blue TBVI, and the SWIR2/NIR TBVI. Once the three shrub-dominated samples were removed from the dataset, site effects in the model were greatly reduced, and all Landsat vegetation

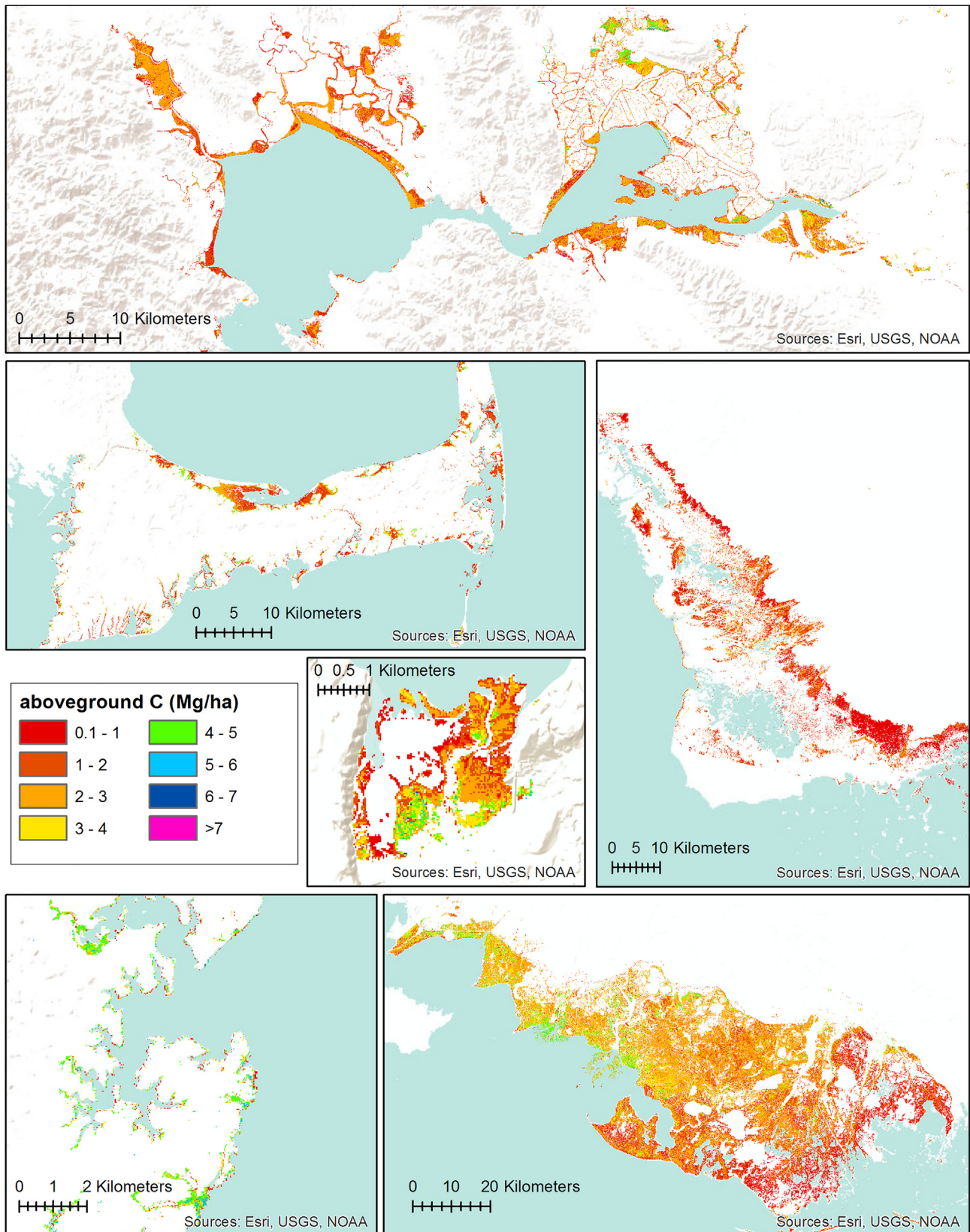


Fig. 9. Tidal marsh aboveground carbon density maps of six study regions, based on the final biomass model (model #2, [table 6](#)) and plant percent carbon content data. Moving from top, left to right: San Francisco Bay, CA, Cape Cod, MA, Everglades, FL, Nisqually NWR, WA, Chesapeake Bay, MD, Terrebonne and St. Mary Parishes, LA.

indices had greater predictive power than any site factor variable, demonstrating the applicability of the model across regions. Of the six indices, SAVI, the Red/Green TBVI and the WDRVI5

have been often used for tidal marsh biomass mapping (Byrd et al., 2016; Langley and Meganigal, 2012; Mishra et al., 2012). The SWIR2/NIR TBVI is the inverse of the Normalized Difference

Table 8

Total and average present day tidal marsh aboveground carbon and uncertainties, by region and wetland type.

Region	Admin Area	C-CAP Class	Mapped Area (ha)	Estimated Area (ha)	+/- s.e.	Mean C (Mg/ha)	+/- s.e.	Total C (Mg)	+/- s.e.
Louisiana	Terrebonne and St. Mary Parishes, LA	Estuarine Emergent	108,787	106,453	4074	1.85	0.003	196,939	7551
		Palustrine Emergent	101,388	116,413	5170	2.67	0.004	310,822	13,834
		Total	210,174	222,866	6582	2.25	0.003	507,761	14,822
Puget Sound	Nisqually National Wildlife Refuge, WA	Estuarine Emergent	611	598	23	1.67	0.015	998	38
		Palustrine Emergent	10	11	1	2.14	0.133	25	1
		Total	621	609	23	1.67	0.015	1023	39
Everglades	Everglades National Park	Estuarine Emergent	38,877	38,043	1456	1.24	0.002	47,173	1806
		Palustrine Emergent	2729	3133	139	0.97	0.003	3039	136
		Total	41,607	41,176	1462	1.22	0.002	50,213	1789
Cape Cod	Barnstable County, Cape Cod, MA	Estuarine Emergent	7831	7663	293	2.01	0.005	15,403	589
		Palustrine Emergent	351	403	18	2.44	0.020	983	44
		Total	8182	8066	294	2.02	0.005	16,386	595
Chesapeake	Anne Arundel County, MD	Estuarine Emergent	1202	1176	45	1.89	0.011	2223	85
		Palustrine Emergent	202	232	10	2.07	0.025	480	21
		Total	1404	1408	46	1.92	0.010	2703	91
SFBay-Brackish/Saline	Bay wetlands in Marin, Sonoma, Napa, Solano, Contra Costa Counties, CA	Estuarine Emergent	16,158	15,811	605	2.03	0.004	32,097	1229
SFBay-Freshwater	Sacramento, San Joaquin Counties, CA	Palustrine Emergent	2122	2436	108	2.13	0.009	5190	231
		Total	18,280	18,248	615	2.04	0.004	37,287	1256

Infrared Index (Hardisky, 1983). The SWIR2/Red TBVI was highly correlated ($r = 0.98$) with the SWIR1/Green TBVI, the inverse of the NDWI (McFeeters, 1996), although it produced better results based on RMSE than the SWIR1/Green TBVI, and so was selected for the final model.

By scaling the field measured average biomass by fractional cover of green vegetation in the pixel, we achieved a more representative estimate of average biomass across the 30 m pixel footprint, which aided model prediction. Using this scaled value as the dependent variable generated lower model error than using unscaled average biomass (RMSE 310 g/m² vs 329 g/m², %NRMSE 10.3% vs. 11%). The object-based classification approach applied here can be costly due to software needs and processing time. However open source programs, such as the python-based RSGISLib (Bunting et al., 2014) can provide a low cost alternative for image processing and classification of green biomass.

The inclusion of Sentinel-1 backscatter within the model was unable to improve the results. Observed increase in RMSE suggests that backscatter was not a reliable predictor of biomass. The inability of the C-band radar to discriminate between varying biomass, despite differences in plant structure suggests the saturation of the received backscatter for the marsh vegetation types. Co-polarization backscatter is increased from vertical structures while cross-polarization is a consequence of volume scattering, often by a canopy structure. Our findings are supported by the result that neither polarization (VV, VH) was a better predictor of biomass than the other, neither within nor between sites, demonstrating the insensitivity of the radar to vegetation structure within the model. This has previously been observed in Louisiana marshes (Ramsey et al., 2013) where local incidence angle was concluded to have a more noticeable effect on backscatter from marshes than polarization. In order to differentiate between marsh types, larger wavelength radar such as L-band radar would be required that is sensitive to the larger components and subsequent biomass of the vegetation. As backscatter of L-band saturates at larger values of biomass, this would be able to discriminate between vegetation

over a greater range of biomass than C-band. Currently, however, no L-band data is consistently available for use within a monitoring system.

The greatest outlier in the VV-VH model (model #11, Table 6) was a sample composed of sawgrass in the Everglades. The recorded biomass value was 92.6 g/m² yet the predicted biomass was 962 g/m² in the VV-VH model (#11, Table 6, Fig. 8). The cause of this was the proximity of the sample site to red mangrove with heights of approximately 250 cm (T. Troxler, personal communication, 05/15/17), which serves as the dominant scatterer detected by the radar. The much larger components and canopy structure of the mangrove in comparison to the marsh vegetation led to a large increase in predicted biomass, as a consequence of increased backscatter. This is synonymous with mixed pixels that are present in optical imagery.

Time and effort in development of the remote sensing dataset used in this study was greatly reduced by taking advantage of the parallel processing and data archive available with Google Earth Engine. The GEE platform allowed for fast access to the massive archive of satellite images, and once the custom code was developed and tested, it allowed for fast, repeatable, automated extraction of and computations on pixel values from such images. Although GEE also contains collections of Sentinel-1 (though incomplete as of May 2017) and NAIP, we primarily used GEE's Landsat imagery collections, which GEE kept current on a more regular basis, to build the Biomass/Remote Sensing dataset (Byrd et al., 2017). Despite the advantages of GEE for building large datasets however, in this study it was determined that some post-processing steps were best performed outside the GEE environment (Supplementary Data S1). The reasons for this included: a. GEE's erratic response time and occasional random server-side failures; and b. processing the dataset locally with relational database management software provides for more flexibility to experiment with many different filtering criteria without suffering the frustrations of slow and/or erratic server response. Judiciously using a combination of local desktop software and GEE's massively

distributed, parallel platform exploits the strengths and avoids the drawbacks of each.

Overall mean carbon densities for tidal marshes across CONUS regions ranged from 1.67 Mg C/ha in the Everglades to 2.25 Mg C/ha in Louisiana. Everglades C density and biomass were on average lower than other regions, likely due to the phosphorus deficiency there that leads to lower productivity of the sawgrass (Childers, 2006). The high carbon density of Louisiana marshes is likely driven by the prevalence of high biomass palustrine emergent marshes, with C density of 2.67 Mg C/ha. Louisiana palustrine marshes had the highest biomass of all regions, while San Francisco Bay brackish/saline marshes had the highest biomass of all estuarine emergent marshes. This distinction might be due to the inclusion of large areas of brackish marsh, which tend to have higher plant biomass than fully saline tidal marshes (Schile et al., 2011).

Through the use of the multivariate delta method for error propagation and inclusion of quantified errors in C-CAP tidal marsh mapped area, we provide an uncertainty analysis method suitable for Tier 2/3 carbon stock assessments. For estuarine emergent marshes we found that broadly across CONUS, estuarine emergent marshes were slightly overrepresented by C-CAP's mapping algorithms and palustrine emergent marshes were slightly underrepresented. Uncertainties in estimated area are related to the proportional areas of commission and omission errors, as well as the mapped area of the classes and number of observations in the validation framework (Olofsson et al., 2014). One unit of mapped estuarine emergent wetland area corresponds to 0.98 ± 0.037 units of estimated area. And one unit of mapped palustrine emergent wetland area corresponds to 1.15 ± 0.051 units of estimated area.

5. Conclusion

In this study we developed a U.S. national-scale remote sensing model of tidal marsh aboveground C stocks based on freely available satellite and airborne imagery and developed with field samples of aboveground biomass and plant %C. In our jurisdictional study regions, estimated C stocks ranged from approximately 1000 Mg in the Nisqually NWR in Washington to over 500,000 Mg in the Terrebonne and St. Mary Parishes in Louisiana. Uncertainties in C stock estimates were calculated through propagation of error in biomass, %C, and C-CAP tidal marsh map area. Remote sensing models such as described here will be used to develop national GHG inventories and aid implementation of projects approved in the voluntary carbon markets. Given global coverage of Landsat, this approach can likely be expanded internationally as well. Although high resolution imagery such as NAIP is not available globally, Landsat-only models will likely provide suitable results, particularly in fully vegetated areas. Newly available global base maps of salt marshes (Mcowen et al., 2017) will also aid global implementation. While archived Landsat imagery can be used for historical estimates of aboveground C flux, moving forward, with the development of a 2015 C-CAP landcover map and continuation of Landsat satellites, future spatially explicit trends can be calculated as well.

Acknowledgements

This research would not be possible without multiple data providers. For San Francisco Bay biomass data, we thank Lisa Schile, Smithsonian Institution, V. Thomas Parker, San Francisco State University, John Callaway, University of San Francisco, Michael Vasey, San Francisco Bay National Estuarine Research Reserve, and Ellen Herbert, Virginia Institute of Marine Science. San Francisco Bay biomass data from 2005 to 2008 were provided through the CALFED Science Program [grant number 4600002970], as part

of the Integrated Regional Wetland Monitoring (IRWM) pilot project, California Bay-Delta Authority Science [grant number 1037], and the National Institute of Climate Change Research (Department of Energy, Coastal Center). For Puget Sound biomass data, we thank Melanie Davis, Isa Woo and Susan De La Cruz, USGS Western Ecological Research Center. For Cape Cod biomass data, we thank Kevin Kroeger, Meagan Gonnee, and Jennifer O'Keefe Suttles, USGS Woods Hole Science Center. For Chesapeake biomass data and plant carbon data, we thank Patrick Megonigal, Meng Lu, and Liza McFarland, Hope Brooks, Bert Drake, Gary Peresta and Andrew Peresta, of the Smithsonian Institution. Additional tissue carbon data were provided by Chris Janousek, Oregon State University. For the Chesapeake data we also acknowledge the National Science Foundation Long-Term Research in Environmental Biology Program [grant numbers DEB-0950080, DEB-1457100, and DEB-1557009], the Department of Energy Terrestrial Ecosystem Science Program [grant numbers DE-FG02-97ER62458, DE-SC0008339] and the Smithsonian Institution. For Everglades biomass data we thank Tiffany Troxler, Florida International University. Everglades biomass data are based upon work supported by the National Science Foundation through the Florida Coastal Everglades Long-Term Ecological Research program [grant number DEB-9910514 (for work from 2000–2006); grant number DBI-0620409 (for work from 2007–2012); and grant number DEB-1237517 (for work from Dec. 2012–2018)]. For Louisiana biomass data, we thank Edward Castañeda, Florida International University. We thank Julie Yee, USGS Western Ecological Research Center, for statistical consultation. Additional San Francisco Bay biomass data (2011 – 2014) were available through a NASA New Investigator Program in Earth Sciences award [grant number NNN10A086I] and a NASA Applied Sciences Program Ecological Forecasting award [grant number NNN14AX16I] to K. Byrd. This research was funded by the NASA Carbon Monitoring System Program [grant number NNN14AY67I], the USGS LandCarbon Program, and the USGS Land Change Science Program. Part of this work was performed at the Jet Propulsion Laboratory, California Institute of Technology. Any use of trade, firm, or product names is for descriptive purposes only and does not imply endorsement by the U.S. Government.

References

- American Carbon Registry, 2017. Approved Methodology for Restoration of California Deltaic and Coastal Wetlands. <<http://americancarbonregistry.org/carbon-accounting/standards-methodologies/restoration-of-california-deltaic-and-coastal-wetlands/california-wetland-restoration-methodology-final-2017.pdf>>.
- Barbour, Burk, Pitts, Gilliam, Schwartz, 1999. *Terrestrial Plant Ecology*. Addison Wesley Longman, Menlo Park, CA.
- Belgiu, M., Drăguț, L., 2016. Random forest in remote sensing: a review of applications and future directions. *ISPRS J. Photogramm. Remote Sens.* 114, 24–31. [10.1016/j.isprsjprs.2016.01.011](https://doi.org/10.1016/j.isprsjprs.2016.01.011).
- Breiman, L., 2001. Random forests. *Machine Learn.* 45, 5–32. doi: [10.1023/a:1010933404324](https://doi.org/10.1023/a:1010933404324).
- Bridgman, S.D., Megonigal, J.P., Keller, J.K., Bliss, N.B., Trettin, C., 2006. The carbon balance of North American wetlands. *Wetlands* 26, 889–916.
- Bunting, P., Clewley, D., Lucas, R.M., Gillingham, S., 2014. The Remote Sensing and GIS Software Library (RSGISLib). *Comput. Geosci.* 62, 216–226. <https://doi.org/10.1016/j.cageo.2013.08.007>.
- Byrd, K., Ballanti, L., Thomas, N., Nguyen, D., Holmquist, J.R., Simard, M., Windham-Myers, L., Schile, L., Parker, V.T., Callaway, J.C., Vasey, M.C., Herbert, E.R., Davis, M., Woo, I., Cruz, S.D.L., Kroeger, K., Gonnee, M., Suttles, J.O.K., Megonigal, P., Lu, M., McFarland, L., Brooks, H., Drake, B., Peresta, G., Peresta, A., Troxler, T., Castañeda, E., 2017. Tidal marsh biomass field plot and remote sensing datasets for six regions in the conterminous United States. *U.S. Geol. Surv. Data Release*. [10.5066/F77943K8](https://doi.org/10.5066/F77943K8).
- Byrd, K.B., O'Connell, J.L., Di Tommaso, S., Kelly, M., 2014. Evaluation of sensor types and environmental controls on mapping biomass of coastal marsh emergent vegetation. *Remote Sens. Environ.* 149, 166–180. <https://doi.org/10.1016/j.rse.2014.04.003>.
- Byrd, K.B., Windham-Myers, L., Leeuw, T., Downing, B., Morris, J.T., Ferner, M.C., 2016. Forecasting tidal marsh elevation and habitat change through fusion of

- Earth observations and a process model. *Ecosphere* 7, e01582. <https://doi.org/10.1002/ecs2.1582>.
- Childers, D.L., 2006. A synthesis of long-term research by the Florida Coastal Everglades LTER Program. *Hydrobiologia* 569, 531–544. <https://doi.org/10.1007/s10750-006-0154-8>.
- Daoust, R., Childers, D., 1998. Quantifying aboveground biomass and estimating productivity in nine Everglades wetland macrophytes using a non-destructive allometric approach. *Aquat. Bot.* 62, 115–133.
- Duarte, C.M., Losada, I.J., Hendriks, I.E., Mazarrasa, I., Marba, N., 2013. The role of coastal plant communities for climate change mitigation and adaptation. *Nat. Clim. Change* 3, 961–968. <https://doi.org/10.1038/nclimate1970>.
- Duarte, C.M., Middelburg, J.J., Caraco, N., 2005. Major role of marine vegetation on the oceanic carbon cycle. *Biogeosciences* 2, 1–8. <https://doi.org/10.5194/bg-2-1-2005>.
- Dube, T., Mutanga, O., 2015. Evaluating the utility of the medium-spatial resolution Landsat 8 multispectral sensor in quantifying aboveground biomass in uMgeni catchment, South Africa. *ISPRS J. Photogramm. Remote Sens.* 101, 36–46. <https://doi.org/10.1016/j.isprsjprs.2014.11.001>.
- Ehrlinger, J., 2015. ggRandomForests: Visually Exploring a Random Forest for Regression. R Package vignette for ggRandomForests package (<https://cran.r-project.org/web/packages/ggRandomForests/index.html>) [Document Version 2]. <<https://arxiv.org/abs/1501.07196v2>>, V2 ed.
- Ghosh, S., Mishra, D.R., Gitelson, A.A., 2016. Long-term monitoring of biophysical characteristics of tidal wetlands in the northern Gulf of Mexico – A methodological approach using MODIS. *Remote Sens. Environ.* 173, 39–58. <https://doi.org/10.1016/j.rse.2015.11.015>.
- Gitelson, A.A., 2004. Wide dynamic range vegetation index for remote quantification of biophysical characteristics of vegetation. *J. Plant Physiol.* 161, 165–173. <https://doi.org/10.1078/0176-1617-01176>.
- Glenn, E.P., Huete, A.R., Nagler, P.L., Nelson, S.G., 2008. Relationship between remotely-sensed vegetation indices, canopy attributes and plant physiological processes: what vegetation indices can and cannot tell us about the landscape. *Sensors* 8, 2136–2160. <https://doi.org/10.3390/s8042136>.
- Goidts, E., Van Wesemael, B., Crucifix, M., 2009. Magnitude and sources of uncertainties in soil organic carbon (SOC) stock assessments at various scales. *Eur. J. Soil Sci.* 60, 723–739. <https://doi.org/10.1111/j.1365-2389.2009.01157.x>.
- Gonzalez-Roglich, M., Swenson, J.J., 2016. Tree cover and carbon mapping of Argentine savannas: scaling from field to region. *Remote Sens. Environ.* 172, 139–147. <https://doi.org/10.1016/j.rse.2015.11.021>.
- Gonzalez, P., Asner, G.P., Battles, J.J., Lefsky, M.A., Waring, K.M., Palace, M., 2010. Forest carbon densities and uncertainties from Lidar, QuickBird, and field measurements in California. *Remote Sens. Environ.* 114, 1561–1575. <https://doi.org/10.1016/j.rse.2010.02.011>.
- Gonzalez Trilla, G., Pratolongo, P., Beget, M.E., Kandas, P., Marcovecchio, J., Di Bella, C., 2013. Relating biophysical parameters of coastal marshes to hyperspectral reflectance data in the Bahía Blanca Estuary, Argentina. *J. Coastal Res.* 29, 231–238. <https://doi.org/10.2112/jcoastres-d-11-00214.1>.
- Google Earth Engine Team, 2017. Google Earth Engine: A Planetary-Scale Platform for Earth Science Data and Analysis <<http://earthengine.google.com>> (accessed 2 November 2017).
- Greaves, H.E., Vierling, L.A., Eitel, J.U.H., Boelman, N.T., Magney, T.S., Prager, C.M., Griffin, K.L., 2016. High-resolution mapping of aboveground shrub biomass in Arctic tundra using airborne lidar and imagery. *Remote Sens. Environ.* 184, 361–373. <https://doi.org/10.1016/j.rse.2016.07.026>.
- Hansen, M.C., Potapov, P.V., Moore, R., Hancher, M., Turubanova, S.A., Tyukavina, A., Thau, D., Stehman, S.V., Goetz, S.J., Loveland, T.R., Kommareddy, A., Egorov, A., Chini, L., Justice, C.O., Townshend, J.R.G., 2013. High-resolution global maps of 21st-century forest cover change. *Science* 342, 850–853. <https://doi.org/10.1126/science.1244693>.
- Hardisky, M.A., 1983. The influence of soil salinity, growth form, and leaf moisture on the spectral radiance of *Spartina alterniflora* canopies. *Photogramm. Eng. Remote Sens.* 49, 77–83.
- Howard, J., Sutton-Grier, A., Herr, D., Kleypas, J., Landis, E., McLeod, E., Pidgeon, E., Simpson, S., 2017. Clarifying the role of coastal and marine systems in climate mitigation. *Front. Ecol. Environ.* 15, 42–50. <https://doi.org/10.1002/fee.1451>.
- Huete, A.R., 1988. A soil-adjusted vegetation index (SAVI). *Remote Sens. Environ.* 25, 295–309. [https://doi.org/10.1016/0034-4257\(88\)90106-X](https://doi.org/10.1016/0034-4257(88)90106-X).
- IPCC, 2003. Intergovernmental Panel on Climate Change Good Practice Guidance for Land Use, Land-Use Change and Forestry. In: Penman, J., Gytarsky, M., Hiraishi, T., Krug, T., Kruger, D., Pipatti, R., Buendia, L., Miwa, K., Ngara, T., Tanabe, K., Wagner, F., (Eds.). <http://www.ipcc-nggip.iges.or.jp/public/gpglulucf/gpglulucf_contents.html>. IPCC, Japan.
- IPCC, 2014. 2013 Supplement to the 2006 IPCC Guidelines for National Greenhouse Gas Inventories: Wetlands. Chapter 4: Coastal Wetlands. In: Hiraishi, T., Krug, T., Tanabe, K., Srivastava, N., Baasansuren, J., Fukuda, M., Troxler, T.G. (Eds.). <<http://www.ipcc-nggip.iges.or.jp/public/wetlands/>>. IPCC, Switzerland.
- Janousek, C.N., Buffington, K.J., Guntenspergen, G.R., Thorne, K.M., Dugger, B.D., Takekawa, J.Y., 2017. Inundation, Vegetation, and Sediment Effects on Litter Decomposition in Pacific Coast Tidal Marshes. *Ecosystems*, 1–15. <https://doi.org/10.1007/s10021-017-0111-6>.
- Kirwan, M.L., Megonigal, J.P., 2013. Tidal wetland stability in the face of human impacts and sea-level rise. *Nature* 504, 53–60. <https://doi.org/10.1038/nature12856>.
- Kuhn, M., 2008. Building predictive models in R using the caret package. *J. Stat. Softw.* 28, 26. <https://doi.org/10.18637/jss.v028.i05>.
- Langley, J.A., Megonigal, J.P., 2012. Field-based radiometry to estimate tidal marsh plant growth in response to elevated CO₂ and nitrogen addition. *Wetlands* 32, 571–578. <https://doi.org/10.1007/s13157-012-0292-x>.
- Lee, J.-S., 1981. Speckle analysis and smoothing of synthetic aperture radar images. *Comput. Graph. Image Process.* 17, 24–32. [https://doi.org/10.1016/S0146-664X\(81\)80005-6](https://doi.org/10.1016/S0146-664X(81)80005-6).
- Li, X., Shao, G., 2014. Object-based land-cover mapping with high resolution aerial photography at a county scale in Midwestern USA. *Remote Sens.* 6, 11372.
- Lobell, D.B., Thau, D., Seifert, C., Engle, E., Little, B., 2015. A scalable satellite-based crop yield mapper. *Remote Sens. Environ.* 164, 324–333. <https://doi.org/10.1016/j.rse.2015.04.021>.
- Lu, M., Caplan, J.S., Bakker, J.D., Adam Langley, J., Mozdzer, T.J., Drake, B.G., Patrick Megonigal, J., 2016. Allometry data and equations for coastal marsh plants 3554 *Ecology* 97. <https://doi.org/10.1002/ecy.1600>.
- Magnussen, S., Köhl, M., Olschofsky, K., 2014. Error propagation in stock-difference and gain-loss estimates of a forest biomass carbon balance. *Eur. J. Forest Res.* 133, 1137–1155. <https://doi.org/10.1007/s10342-014-0828-0>.
- McCombs, J.W., Herold, N.D., Burkhalter, S.G., Robinson, C.J., 2016. Accuracy assessment of NOAA coastal change analysis program 2006–2010 land cover and land cover change data. *Photogramm. Eng. Remote Sens.* 82, 711–718. [https://doi.org/10.1016/S0099-1112\(16\)30122-7](https://doi.org/10.1016/S0099-1112(16)30122-7).
- McFeeters, S.K., 1996. The use of the Normalized Difference Water Index (NDWI) in the delineation of open water features. *Int. J. Remote Sens.* 17, 1425–1432. <https://doi.org/10.1080/01431169608948714>.
- McLeod, E., Chmura, G.L., Bouillon, S., Salm, R., Björk, M., Duarte, C.M., Lovelock, C.E., Schlesinger, W.H., Silliman, B.R., 2011. A blueprint for Blue Carbon: toward an improved understanding of the role of vegetated coastal habitats in sequestering CO₂. *Front. Ecol. Environ.* 9, 552–560. <https://doi.org/10.1890/110004>.
- Mcowen, C.J., Weatherdon, L.V., Bochove, J.-W.V., Sullivan, E., Blyth, S., Zockler, C., Stanwell-Smith, D., Kingston, N., Martin, C.S., Spalding, M., Fletcher, S., 2017. A global map of saltmarshes. *Biodivers. Data J.* 5. <https://doi.org/10.3897/BDJ.5.e11764>.
- Mishra, D.R., Cho, H.J., Ghosh, S., Fox, A., Downs, C., Merani, P.B.T., Kirui, P., Jackson, N., Mishra, S., 2012. Post-spill state of the marsh: remote estimation of the ecological impact of the Gulf of Mexico oil spill on Louisiana Salt Marshes. *Remote Sens. Environ.* 118, 176–185. <https://doi.org/10.1016/j.rse.2011.11.007>.
- Mutanga, O., Adam, E., Cho, M.A., 2012. High density biomass estimation for wetland vegetation using WorldView-2 imagery and random forest regression algorithm. *Int. J. Appl. Earth Obs. Geoinf.* 18, 399–406. <https://doi.org/10.1016/j.jag.2012.03.012>.
- Mutanga, O., Skidmore, A.K., 2004. Narrow band vegetation indices overcome the saturation problem in biomass estimation. *Int. J. Remote Sens.* 25, 3999–4014. <https://doi.org/10.1080/01431160310001654923>.
- Nagler, P.L., Glenn, E.P., Thompson, T.L., Huete, A., 2004. Leaf area index and normalized difference vegetation index as predictors of canopy characteristics and light interception by riparian species on the Lower Colorado River. *Agric. For. Meteorol.* 125, 1–17. <https://doi.org/10.1016/j.agrformet.2004.03.008>.
- NOAA Office for Coastal Management, 2015. NOAA Coastal Change Analysis Program (C-CAP) Regional Land Cover Database. Data collected 1995–present. Data accessed at www.coast.noaa.gov/digitalcoast/data/ccapregional, Charleston, SC.
- Ollinger, S.V., 2011. Sources of variability in canopy reflectance and the convergent properties of plants. *New Phytol.* 189, 375–394.
- Olofsson, P., Foody, G.M., Herold, M., Stehman, S.V., Woodcock, C.E., Wulder, M.A., 2014. Good practices for estimating area and assessing accuracy of land change. *Remote Sens. Environ.* 148, 42–57. <https://doi.org/10.1016/j.rse.2014.02.015>.
- Parker, V.T., Callaway, J., Schile, L., Vasey, M., Herbert, E., 2012. Tidal vegetation: spatial and temporal dynamics. In: Palaima, A. (Ed.), *Ecology, Conservation, and Restoration of Tidal Marshes: the San Francisco Estuary*. University of California Press, Berkeley, CA, pp. 97–111.
- Parker, V.T., Callaway, J.C., Schile, L.M., Vasey, M.C., Herbert, E.R., 2011. Climate Change and San Francisco Bay-Delta Tidal Wetlands. *San Francisco Estuary and Watershed Science* 9. <https://escholarship.org/uc/item/8j20685w>.
- Pekel, J.-F., Cottam, A., Gorelick, N., Belward, A.S., 2016. High-resolution mapping of global surface water and its long-term changes. *Nature* 540, 418–422. <https://doi.org/10.1038/nature20584>.
- Pendleton, L., Donato, D.C., Murray, B.C., Crooks, S., Jenkins, W.A., Sifleet, S., Craft, C., Fourqurean, J.W., Kauffman, J.B., Marbà, N., Megonigal, P., Pidgeon, E., Herr, D., Gordon, D., Baldera, A., 2012. Estimating global “Blue Carbon” emissions from conversion and degradation of vegetated coastal ecosystems. *PLoS ONE* 7, e43542. <https://doi.org/10.1371/journal.pone.0043542>.
- Pettorelli, N., Laurance, W.F., O'Brien, T.G., Wegmann, M., Nagendra, H., Turner, W., 2014. Satellite remote sensing for applied ecologists: opportunities and challenges. *J. Appl. Ecol.* 51, 839–848. <https://doi.org/10.1111/1365-2664.12261>.
- Piñeiro, G., Perelman, S., Guerschman, J.P., Paruelo, J.M., 2008. How to evaluate models: Observed vs. predicted or predicted vs. observed? *Ecol. Model.* 216, 316–322. <https://doi.org/10.1016/j.ecolmodel.2008.05.006>.
- Ramsey III, E., Rangoonwala, A., Chi, Z., Jones, C.E., Bannister, T., 2014. Marsh Dieback, loss, and recovery mapped with satellite optical, airborne polarimetric radar, and field data. *Remote Sens. Environ.* 152, 364–374. <https://doi.org/10.1016/j.rse.2014.07.002>.
- Ramsey, E., Rangoonwala, A., Bannister, T., 2013. Coastal Flood inundation monitoring with satellite C-band and L-band synthetic aperture radar data.

- JAWRA J. Am. Water Resources Assoc. 49, 1239–1260. <https://doi.org/10.1111/jawr.12082>.
- Roy, D.P., Kovalsky, V., Zhang, H.K., Vermote, E.F., Yan, L., Kumar, S.S., Egorov, A., 2016. Characterization of Landsat-7 to Landsat-8 reflective wavelength and normalized difference vegetation index continuity. *Remote Sens. Environ.* 185, 57–70. <https://doi.org/10.1016/j.rse.2015.12.024>.
- Schalles, J.F., Hladik, C.M., Lynes, A.A., Pennings, S.C., 2013. Landscape estimates of habitat types, plant biomass, and invertebrate densities in a Georgia salt marsh. *Oceanography* 26, 88–97.
- Schile, L.M., Callaway, J.C., Parker, V.T., Vasey, M.C., 2011. Salinity and Inundation Influence Productivity of the Halophytic Plant *Sarcocornia pacifica*. *Wetlands* 31, 1165–1174. <https://doi.org/10.1007/s13157-011-0227-y>.
- Shoko, C., Mutanga, O., Dube, T., 2016. Progress in the remote sensing of C3 and C4 grass species aboveground biomass over time and space. *ISPRS J. Photogramm. Remote Sens.* 120, 13–24. <https://doi.org/10.1016/j.isprsjprs.2016.08.001>.
- Thenkabail, P.S., Enclona, E.A., Ashton, M.S., Van Der Meer, B., 2004. Accuracy assessments of hyperspectral waveband performance for vegetation analysis applications. *Remote Sens. Environ.* 91, 354–376.
- Tramontana, G., Ichii, K., Camps-Valls, G., Tomelleri, E., Papale, D., 2015. Uncertainty analysis of gross primary production upscaling using Random Forests, remote sensing and eddy covariance data. *Remote Sens. Environ.* 168, 360–373. <https://doi.org/10.1016/j.rse.2015.07.015>.
- Troxler, T., Childers, D.L., 2017. Sawgrass above ground biomass from the Taylor Slough, Everglades National Park (FCE), South Florida from August 1999 to Present, Florida Coastal Everglades long term ecological research network (http://fcelter.fiu.edu/data/core/metadata/?datasetid=LT_PP_Rubio_001).
- U.S. Fish and Wildlife Service, 2014. National Wetlands Inventory website. U.S. Department of the Interior, Fish and Wildlife Service, Washington, D.C..
- USDA Farm Service Agency, 2017. National Agriculture Imagery Program (NAIP). <<https://www.fsa.usda.gov/programs-and-services/aerial-photography/imagery-programs/naip-imagery/index>>.
- USDA NRCS, 2017. The PLANTS Database (<http://plants.usda.gov>, 9 May 2017). National Plant Data Team, Greensboro, NC 27401-4901 USA.
- USEPA, 2017. Inventory of US greenhouse gas emissions and sinks: 1990–2015. Environmental Protection Agency 2017. <<https://www.epa.gov/ghgemissions/inventory-us-greenhouse-gas-emissions-and-sinks-1990-2015>>.
- Vasquez, E.A., Glenn, E.P., Brown, J.J., Guntenspergen, G.R., Nelson, S.G., 2005. Salt tolerance underlies the cryptic invasion of North American salt marshes by an introduced haplotype of the common reed *Phragmites australis* (Poaceae). *Mar. Ecol. Prog. Ser.* 298, 1–8. <https://doi.org/10.3354/meps298001>.
- Ver Hoef, J.M., 2012. Who invented the delta method? *The Am Statistic.* 66, 124–127. <https://doi.org/10.1080/00031305.2012.687494>.
- Verified Carbon Standard, 2015. VM0033. Approved Methodology for Tidal Wetland and Seagrass Restoration. <http://database.v-c-s.org/sites/vcs.benfredaconsulting.com/files/VM0033%20Tidal%20Wetland%20and%20Seagrass%20Restoration%20v1.0%2020%20NOV%202015_0.pdf>.
- Vermote, E., Justice, C., Claverie, M., Franch, B., 2016. Preliminary analysis of the performance of the Landsat 8/OLI land surface reflectance product. *Remote Sens. Environ.* 185, 46–56. <https://doi.org/10.1016/j.rse.2016.04.008>.
- Wyllie, L., Sutton-Grier, A.E., Moore, A., 2016. Keys to successful blue carbon projects: lessons learned from global case studies. *Mar. Policy* 65, 76–84. <https://doi.org/10.1016/j.marpol.2015.12.020>.
- Yuan, F., Bauer, M.E., 2006. Mapping impervious surface area using high resolution imagery: A comparison of object-based and per pixel classification, American Society for Photogrammetry and Remote Sensing - Annual Conference of the American Society for Photogrammetry and Remote Sensing 2006: Prospecting for Geospatial Information Integration, Reno, NV, pp. 1667–1674.